In-ice measurements of full spectral angular radiance distribution using a 360-degree camera

Raphaël Larouche[1,2,*], Bastian Raulier[1,3,*], Christian Katlein[4], Simon Lambert-Girard[1], Simon Thibault[2], Marcel Babin[1]

[1]Takuvik International Research Laboratory, Université Laval (Canada) & CNRS (France), Département de Biologie and Québec-Océan, Université Laval, Pavillon Alexandre-Vachon 1045, avenue de la Médecine, Local 2064, G1V 0A6, Canada
[2]Centre d'optique, photonique et laser (COPL), Université Laval, Québec, QC, Canada
[3]CERVO Brain Research Center, Québec, G1J 2G3, Canada
[4]Alfred-Wegener-Institut Helmholtz-Zentrum für Polar und Meeresforschung, Bremerhaven, Germany
*These authors contributed equally to this work.

This preprint submitted to EarthArXiv has not been peer-reviewed yet. It is a first version of the manuscript and subsequent version may include different content.

Correspondence to: Raphaël Larouche (raphael.larouche@takuvik.ulaval.ca)

Abstract. A better understanding of the radiative transfer of solar visible light within sea ice is crucial to study the Arctic energy balance and marine ecosystems. In this work, we showcase the utilization of a compact, consumer-grade 360-degree camera for measuring the in-ice spectral angular radiance distribution. This novel technique allows for the instantaneous acquisition of all radiometric quantities at a given depth with a compact, non-intrusive probe. This gives the opportunity to monitor the light field structure (mean cosines) from the atmosphere to the underlying ocean beneath ice. In this study, we report vertical profiles of the light field geometric distribution measured at two sites representative of distinct ice types: High Arctic multi-year ice and Chaleur Bay (Quebec) land fast first-year ice. We show that it is possible to empirically retrieve the depth-resolved internal optical properties by matching simulated profiles of spectral irradiances calculated with the HydroLight radiative transfer model to the observed profiles. As reported in other studies, the inverted reduced scattering coefficients were high (25.5 m^{-1}, 37.5 m^{-1}) in the first 20 centimeters for both sites (High Arctic, Chaleur Bay) and lower in the interior part of the ice (0.8 to 4.8 m^{-1}, 2.8 to 7.2 m^{-1}). Finally, due to the underdetermined nature of the inversion problem, we emphasize the importance of using the similarity parameter that considers the absorption and reduced scattering coefficients.

1 Introduction

The Arctic Ocean has undergone major transformations in the last few decades as perennial sea ice has largely been replaced by thinner first-year ice (Comiso, 2002; Maslanik et al., 2011) and as a significant decrease of the ice extent was observed (Serreze et al., 2007; Comiso et al., 2008). These changes have critical impacts on the atmosphere-ice-ocean system, especially during the spring to summer melting season as sea ice is transformed in a highly inhomogeneous cover of snow, bare ice, melt

ponds and leads (Perovich et al., 2002; Frey et al., 2011; Ehn et al., 2011; Katlein et al., 2016; Horvat et al., 2020). Seasonal ice has higher melt pond fraction (Hunke et al., 2013; Eicken et al., 2004; Li et al., 2020) and enables more solar shortwave radiation transmission and deposition through absorption (Nicolaus et al., 2012). This new energy partition heats sea ice and the underlying ocean leading to accelerated ice melt within a positive feedback loop (Curry et al., 1995; Perovich et al., 2008) which impacts regional arctic climates. Thinner ice cover promotes significant under-ice phytoplankton blooms earlier in the season (Arrigo et al., 2012, 2014; Mundy et al., 2009).

The amount of shortwave radiation scattered or absorbed by a given medium is determined by its inherent optical properties (IOPs). These material properties determine the propagation of light throughout the medium, which in bulk are often described by the apparent optical properties (AOPs) like albedo and transmittance (Light et al., 2003a). The apparent optical properties of sea ice exhibit large seasonal and spatial variability due to the mosaic-like surface structure and variations in the physical properties of sea ice (Perovich et al., 1998; Matthes et al., 2020; Katlein et al., 2019). An improved understanding of the links between structural and optical properties is needed to predict the impacts of sea ice transformation on arctic ecosystems. While surface AOPs such as albedo (Perovich et al., 2002; Grenfell and Perovich, 2004; Ehn et al., 2006) and bulk transmittance (Perovich et al., 1993, 1998; Nicolaus and Katlein, 2013; Katlein et al., 2015) have been well documented over the past decades, very few in situ optical measurements have been made inside sea ice. These additional measurements are needed to better constrain optical models. Vertical profiles of planar irradiances have been acquired with large probes—which are prone to self-shadowing—lowered into bore holes of 5 to 10 cm in diameter (Ehn et al., 2008b; Light et al., 2008; Xu et al., 2012a; Light et al., 2015) or, alternatively, measured by digging holes from below the sea ice which required a diver (Ehn et al., 2008a). Efforts to reduce perturbations on sea ice physical properties were made with the development of vertical arrangements of fiber optics (Wang et al., 2014) or photodiodes having their normal axis 90° rotated from zenith direction (Katlein et al., 2021) taking autonomous measurements of irradiance in refrozen holes. To acquire either planar or scalar irradiance is not sufficient to fully describe the internal light field because both quantities average the angular distribution of radiance. These measurements lack information about the light field geometry within the ice. Measurements of radiance have previously been collected in sea ice using single-direction radiance meters with a 3˚ to 7˚ field of view (FOV) (Perovich et al., 1998; Pegau and Zaneveld, 2000; Xu et al., 2012a). This approach is, however, time consuming as holes must be drilled in different zenith directions and the radiometer rotated for azimuth acquisitions to get a full radiance distribution at a rather low angular resolution and high structural disturbance by the sampling method. All radiometric quantities and, therefore all AOPs, can be calculated from angular radiance distribution over 4 π steradians (Mobley, 1994).

Here we present a solution to measure radiance using a camera assembly whose pixels instantaneously resolve angular radiance distributions over a large portion of 4 π steradians. Such instruments have been used to study radiative transfer in the ocean (Smith et al., 1970; Voss and Chapin, 2005, 1992; Voss and Zibordi, 1989; Wei et al., 2012; Antoine et al., 2013). Of these radiometers, the smallest one was packaged inside a 9.6 x 26 cm (diameter x length) case (Antoine et al., 2013), making it

unsuitable for in-ice applications due to self-shadowing and the large hole that must be drilled. Recently, lens and imaging sensor miniaturization has led to the commercialization of compact fisheye cameras. One of them is the Insta360 ONE (see Fig. 1c. Insta360, Arashi Vision Inc.). After rigorous radiometric calibrations (Larouche et al., n.d. in prep) this low-cost camera becomes an easy-to-use instrument for measuring radiance distributions within sea ice. This paper presents the first vertical profiles of the angular radiance distributions inside sea ice at high angular resolution. The measurements were acquired in two different field sites, one in the High Arctic close to the geographic North Pole and the other one in Chaleur Bay in the province of Quebec. First, we provide the vertical profile of the radiometric quantities for High Arctic multi-year sea ice (spectral angular radiance distributions and their corresponding irradiances) and then some depth resolved AOPs. For both field sites, we present IOPs inferred by empirically identifying the radiometric quantities calculated with the HydroLight (HL) radiative transfer simulation software that best fit the observed ones. Finally, we present an analysis of the impact of the shape of the phase function on the in-ice radiance and demonstrate a study of the errors of the IOPs inversion generated by our method.

2 Materials and methods

2.1 Field measurements

High-Artic field measurements were conducted near the geographic north pole on August 31, 2018 (89° 25.21'N, 63° 08.67'E) during the AO18 expedition with the research icebreaker *Oden* (see Fig. 1a and 1d). The multi-year (MY) sea ice at the site was 200 ± 5 cm thick with a freeboard of 17 ± 5 cm and covered by 2 cm of fresh dry snow. Profiles of angular radiance distributions were collected inside a 5 cm diameter hole, snugly fitting the camera case. Measurements were taken at a vertical resolution of 20 cm. At the measurements site, three sensors RAMSES-ACC-VIS (TriOS GmbH, Rastede, Germany) were positioned to acquire the downward, reflected, and transmitted (under sea ice) planar irradiance (Fig. 1c). The hyperspectral irradiance sensors acquired wavelengths between 320-950 nm with increments of 3.3 nm (Nicolaus et al., 2010; Katlein et al., 2021). As for the atmospheric conditions, the incoming radiation was highly diffuse (see Fig. 1a) because of the presence of low stratus clouds (often observed in the High Arctic) and the low sun elevation.

A second field campaign took place in Chaleur Bay, Quebec, Canada (48° 06.47' N, 66° 26.97' W) on March 23, 2022 (see Fig. 1b and 1d). This place is located in the the Gulf of St. Lawrence Gulf where seasonal sea ice forms during winter. The sampling site was chosen close to land. Four different holes were drilled at the site. The thickness of the ice varied from 72 ± 5 cm to 80 ± 5 cm, while freeboard was within 15 ± 5 cm to 20 ± 5 cm. Vertical profiles of angular radiance distribution were acquired in each hole with depth increments of 5 cm. The Compact-Optical Profiling System (C-OPS, Biospherical Instruments Inc.) was used to continuously collect the downwelling irradiance (19 spectral bands between 380 and 875 nm; (Morrow et al., 2010)) as surface reference during in-ice camera measurements. As seen from Fig. 1b, clear sky conditions prevailed at the sampling site with a few passing clouds. The sun elevation at the time of measurements was 42.9°.

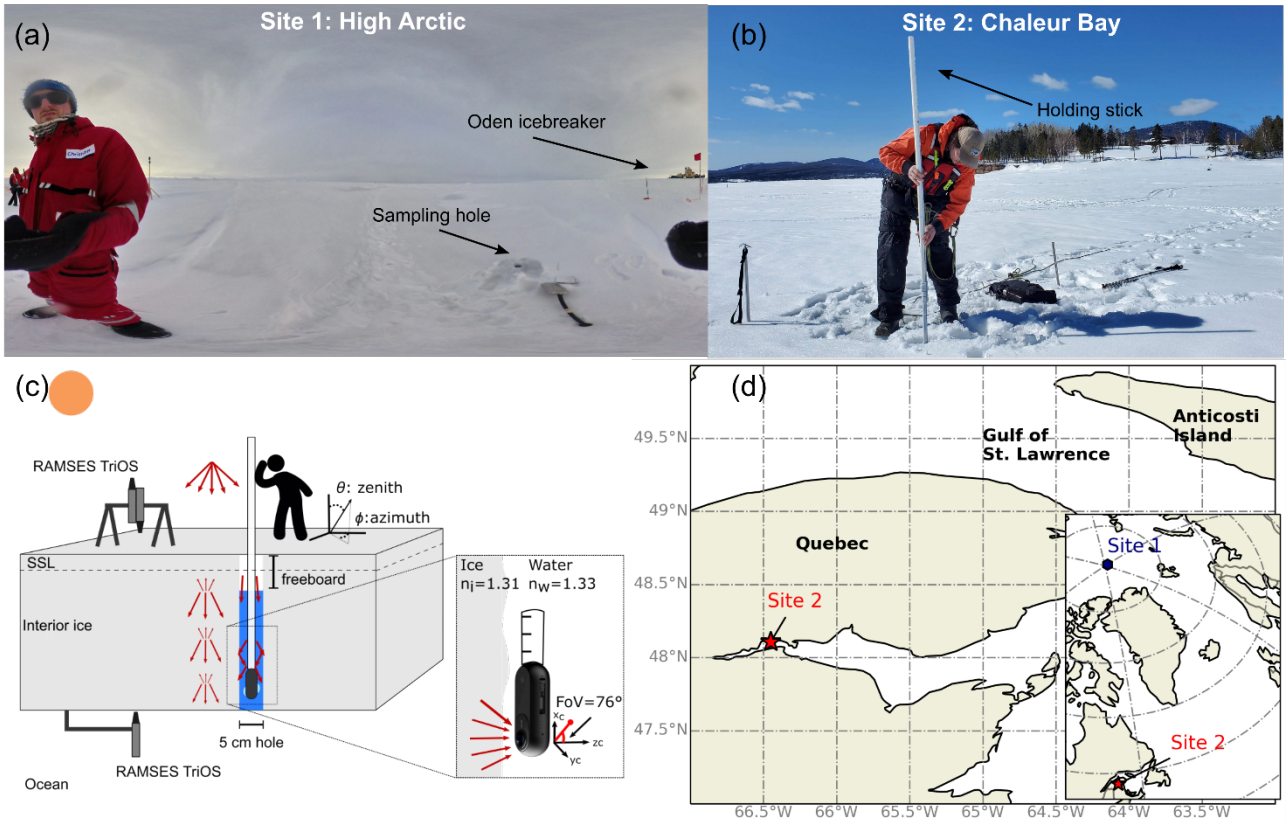

Figure 1: Field sampling of the depth-resolve angular radiance distribution inside sea ice using the commercial 360-degrees camera Insta360 ONE. In (a), the image taken with the omnidirectional camera of the site near the North Pole in High Arctic (89° 25.21'N, 63° 08.67'E) shows a sun near the horizon and the presence of cloud, which are conditions often producing isotropic atmospheric incident light angular distribution. (b) Sampling site at Chaleur Bay (48° 06.47'N, 66° 26.97'W), Quebec, Canada, with completely different meteorological conditions (sunny day with very few clouds) where we can see the operator inserting inside sea ice the graduated stick with the camera attached to the tip. Both sampling sites are geographically positioned on the map in (d). Schematic of the acquisition method is illustrated in (c) with the camera inserted in the drilled hole (5 cm in diameter) for image capture at multiple depths. In High Arctic, RAMSES-ACC-VIS sensors were used to measure irradiance at the surface and below sea ice, while a C-OPS irradiance sensor was used (at surface only) at Chaleur Bay.

2.2 Camera description and capture modes

The Insta360 ONE commercial omnidirectional camera (see Fig. 1c) has a diameter of 5 cm, includes two fixed-aperture ($f\# = 2.2$) fisheye lenses covering each solid angles of $2\,\pi$ steradians (in air). The imaging detectors are two Sony CMOS sensors (1/2.3" format, 6.95 mm in diagonal) with a total number of 3456 x 3456 pixels (12 mega-pixel) covered in a repeated Bayer mosaic of 3 waveband filters (conventional RGB). The analog to digital converter (ADC) has a resolution of 14 bits (16 384 possible values). An important feature of this camera is the availability of raw image capture at sensor-level allowing

radiometry utilization. The camera can be purchased with a waterproof enclosure, and thus can be used in wet environments such as holes drilled inside sea ice. With the camera attached to a depth-graduated stick, the acquisition strategy was to start a timer – set to the maximum value of 10 s – and then quickly lower the camera to the desired location inside the drill hole (see Fig. 1c). With the raw option activated, the images were saved to a microSD card in Digital Negative format (DNG, developed by Adobe).

2.3 Image processing, radiometry, and optical properties

The image processing pipeline starts by performing demosaicing, where each spectral RGB component is downsampled from the raw image. Then, after dark correction, we apply the measurement equation with the proper calibration variables – considering in-air/in-water utilization – to transform the digital numbers of each spectral i band into effective spectral radiance values $\bar{L}_i$ [W sr^{-1} m^{-2} nm^{-1}]. For the dark subtraction, an average of the unexposed part of the CMOS sensor was used. The measurement equation as well as the calibration and characterization methodologies of the variables involved in this formula are fully described in Larouche et al. (n.d. in prep). Lastly, the pixel wise $\bar{L}_i(\theta_c, \phi_c)$ – with θ_c, ϕ_c being the spherical coordinates with respect to the optics reference systems – are re-mapped on a zenith (θ) and azimuth (ϕ) grid of 1° in angular resolution.

The integration of the radiant energy in every direction (over a hemispherical solid angle) weighted by $\cos\theta$ gives the equivalent planar irradiance. This radiometric quantity is used for energy budget calculation influencing sea ice mass balance (Jin et al., 1994; Ebert et al., 1995; Light et al., 2015). Scalar irradiance is a more appropriate radiometric quantity for photosynthetically active organisms as they are equally sensitive to every photon direction (Katlein et al., 2014). Both quantities can be calculated given:

$$E(z,\lambda) = \int_0^{2\pi} \int_{\theta_1}^{\theta_2} f(z,\theta,\phi) d\theta d\phi \quad (1)$$

with $E(z,\lambda)$ [W m^{-2} nm^{-1}] being the irradiances at different depth z [cm]. For a planar irradiance of (E_d or E_u), $f(z,\theta,\phi) = \bar{L}_i(z,\theta,\phi)\,|\cos\theta|\sin\theta$. With a scalar irradiance of (E_d^o or E_u^o), the integrand function is $f(z,\theta,\phi) = \bar{L}_i(z,\theta,\phi)\sin\theta$. For the radiation coming from either downward or upward directions (d and u subscripts), the zenithal integration boundaries are set to $[\theta_1,\theta_2] = [0,\pi/2]$ and $[\theta_1,\theta_2] = [\pi/2,\pi]$, respectively. We used the composite Simpson's rule for the numerical integrations in both dimensions (θ, ϕ). However, before calculating the irradiances, any missing radiance values—resulting from the in-water reduced FOV—had to be extrapolated. This extrapolation was accomplished through a 5th degree Legendre polynomial fit on the azimuthally averaged spectral radiance (see appendix A). The attenuation of the planar irradiance travelling in the downward hemisphere with depth is calculated by:

$$K_d(z,\lambda) = -1/E_d(z,\lambda) \cdot dE_d(z,\lambda)/dz \quad (2)$$

where $K_d(z,\lambda)$ [m^{-1}] is the depth resolved downwelling diffuse attenuation coefficients. This function gives the rate at which light gets attenuated due to scattering and absorption. In addition to the IOPs, $K_d(z,\lambda)$ coefficients are influenced by the environmental conditions such as the position of the sun in the sky, therefore it is an apparent optical property. From the depth measurements of the downward planar irradiance, we used the second order central difference for the numerical calculations of the diffuse attenuation coefficients.

The average cosine links together the planar and scalar irradiances for the downward and upward light field according to:

$$\bar{\mu}_d(z,\lambda) = \frac{E_d(z,\lambda)}{E_d^o(z,\lambda)} \qquad \bar{\boldsymbol{\mu}}_{\boldsymbol{u}} = \frac{\boldsymbol{E_u(z,\lambda)}}{\boldsymbol{E_u^o(z,\lambda)}} \tag{3}$$

where $\bar{\mu}_d$ and $\bar{\mu}_u$ are respectively the average cosines for downwelling and upwelling light field. They are geometric indices of the radiance angularly distributed and are controlled, in part, by the medium inherent optical properties. For μ_d, values of 0.5 and 1.0 correspond to isotropic and completely downward light fluxes respectively. The average cosine of the complete angular radiance distribution is calculated from the following relationship:

$$\bar{\mu}(z,\lambda) = \langle \cos\theta \rangle = \frac{\int_0^{2\pi}\int_0^{\pi} \bar{L}_i(z,\theta,\phi)\cdot\cos\theta\cdot\sin\theta\, d\theta d\phi}{\int_0^{2\pi}\int_0^{\pi} \bar{L}_i(z,\theta,\phi)\cdot\sin\theta\, d\theta d\phi} = \frac{E_d(z,\lambda) - E_u(z,\lambda)}{E_o(z,\lambda)} \tag{4}$$

where $\bar{\mu}$ and E_o [W m^{-2} nm^{-1}] are respectively the average cosine and the scalar irradiance of the 4π steradians sphere. Apart from understanding how the geometry of the light field evolves with depth, paring the average cosine $\bar{\mu}(z,\lambda)$ with the net irradiance $E_d(z,\lambda) - E_u(z,\lambda)$, gives an estimation of the depth resolved absorption coefficient $a(z,\lambda)$ under conservation of energy (Mobley, 1994):

$$a(z,\lambda) = -\bar{\mu}(z,\lambda)\cdot\frac{d}{dz}[\ln(E_d(z,\lambda) - E_u(z,\lambda))] \tag{5}$$

This equation is also known as Gershun's law and resolves the transport equation explicitly assuming negligible contributions from inelastic scattering or internal sources. It was used to infer absorption coefficients in a water environment with uncertainty in the range of 21 % (Voss, 1989).

2.4 Inherent optical properties inversion

There is a wide variety of models used to solve the radiative transfer equation (RTE) (Preisendorfer, 1965) in scattering media. In this study we chose the HydroLight (Mobley, 1994) radiative transfer model which solves the RTE using the invariant embedding technique. This model takes as input any depth dependant set of IOPs and sky incident irradiance. This implementation is particularly powerful because it enables the use of any depth dependant phase function.

The two measurement sites were treated differently in HydroLight because they differ with many respects. For the High Arctic, the simulations were executed using a diffuse sky illumination to simulate the stratus cloud cover that day (see. Fig. 1a). In the High Arctic, the sea floor reflectance effect was neglected, the water column being simulated as infinitely deep. For the

measurements taken under clear sky in Chaleur Bay. The geographic coordinates of the sampling site and the UTC time of measurement were used to calculate the proper zenithal angle of the sun within the model. Then, to properly represent the shallow waters of the bay, the simulations were run with a water column of 5 meters beneath the ice cover with a sea floor reflectance of 10%. This reflectance value is representative of coastal oceanic bottom reflectance in Chaleur Bay. For both measurement sites, the downwelling spectral irradiance measurement at the surface was used as input in the simulations, and the ice stack was split in 20 centimeter thick slabs. This separation was a compromise, as it was sufficiently thin to represent the main vertical structure variation of the ice (surface scattering layer, drained layer, and interior layer) yet coarse enough to avoid an overfitting of IOPs. We considered each simulated layer with a refractive index of 1. The discontinuity in a medium results in a change of direction of photons, corresponding to scattering. In the present case, the many irregularities in sea ice results in a high scattering coefficient and frequent changes of direction by photons. These frequent redirections quickly destroy the information of the incident radiance distribution and the effect of the interfaces. Therefore, the air/snow, the snow/ice, and ice/sea water interfaces are simulated as only additional scattering events. This simpler treatment avoids the problem that arises from a change in refractive index in a strongly scattering medium: an index change coupled with isotropic radiance leads to large total internal refraction creating zones of higher irradiances (hot zone) in the simulations near the reflecting interfaces.

The measurement of the radiance profile does not directly give a lot of information about the IOPs of the medium. Estimating those optical parameters is quite challenging because the problem is underdetermined. We investigated the use of numerical fitting methods, such as the Nelder-Mead downhill simplex algorithm, but none of them provide satisfactory results. Therefore, we search by trial and error the set of IOPs that provided the best fit between calculated irradiance profiles and measured ones (E_d, E_u and E_o), and thereby obtained the absorption, scattering and the phase function anisotropy coefficients (a, b & g). This manual fit always followed the same procedure: first, the scalar irradiance profile fit (E_o) at 480 nm was obtained by adjusting the corresponding absorption coefficient; and second, the 480 nm upward and downward vector irradiance profiles were fitted by modifying the scattering and anisotropy coefficients of the phase function. The absorption and scattering coefficients drive both the absorbed and the backscattered energy, and the anisotropy coefficient drive the front/back scattered ratio (Jacques, 2013). Those two steps were repeated until a satisfactory fit was obtained for that wavelength. Assuming that the scattering coefficient is independent of wavelength, only the absorption coefficients are modified to extend the fit to the other two channels (540 and 600 nm). The stopping criterion was reached when there was no further improvement of the relative error between modeled and measured irradiances.

This procedure, although leading to profiles very close to those observed, does not claim to recover the exact inherent optical properties of the ice. Indeed, this procedure only allows finding one of the solutions among a larger ensemble. This ensemble is defined as the sets of inherent optical properties leading to the same irradiance gradient. We can imagine two different media, one very absorbent but with low scattering and another with little absorption but high scattering will both give rise to

the same gradient. Van de Hulst introduced in 1980 a useful equation, Eq. (6), to compare the pairs of IOPs that give rise to the same gradient (van de Hulst, 1980).

$$S = [1 + (b/a) \cdot (1 - g)]^{-\frac{1}{2}} \quad (6)$$

where S is the similarity parameter. This invariant is the geometric mean of the two first moments of the diffusion pattern. The latter being valid for thick scattering slabs far from boundaries, it has already been used to compare set of IOPs by Light and Ehn (Ehn et al., 2008b; Light et al., 2004). For two layers that have constant absorption coefficient, the a in Eq. (**6**) vanished which give the following parameter

$$b' = b(1 - g) \quad (7)$$

with b' corresponding to the reduced scattering coefficient, another similarity parameter. This quantity is often used for comparisons of inverted IOPs in sea ice as two regions with the same reduced scattering coefficients are identical in term of scattering.

2.5 Impact of the phase function shape

The phase function describes the density of probability that a photon gets redirected at a certain angle after a single scattering event. The angular distribution of the surrounding light field is affected by the phase function when limited scattering occurs in the medium (Jacques, 2013). We ran HydroLight simulations with the phase functions having diverse shapes to assess their impact on the difference between the simulated and measured radiances. For radiative transfer simulations in sea ice, the Henyey-Greenstein function (Henyey and Greenstein, 1941) is usually selected (Mobley et al., 1998; Light et al., 2004, 2008, 2003a, 2015; Petrich et al., 2012):

$$p_{HG}(\theta, g_{HG}) = \frac{1}{4\pi} \cdot \frac{1 - g_{HG}^2}{(1 + g_{HG}^2 - 2g_{HG}\cos\theta)^{\frac{3}{2}}}. \quad (8)$$

The Henyey-Greenstein equation $p_{HG}(\theta, g)$ [sr^{-1}] has the asymmetry parameter g as the first moment, which can vary between 0 (isotropic) and 1 (complete forward). The first moment g of any phase function is found by:

$$g = \langle \cos\theta \rangle = 2\pi \int_0^{\pi} p(\theta) \cos\theta \sin\theta d\theta \, . \quad (9)$$

The Henyey-Greenstein equation was proposed from observations of the scattering by interstellar matter and has only one degree of freedom. Thus, it fails to accurately model complex phase functions; the latter being physically determined by the shape, the size distributions, and the relative refractive indexes of the scatterers. To allow more flexibility, a phase function that can fit the first three moments was proposed (Kattawar, 1975):

$$p_{TTHG}(\theta, \alpha, g_1, g_2) = \alpha \cdot p_{HG}(\theta, g_1) + (1 - \alpha) \cdot p_{HG}(\theta, -g_2) \quad (10)$$

where $p_{TTHG}(\theta, \alpha, g_1, g_2)$ [sr^{-1}] is the total phase function, α is the weight for the forward directed Henyey-Greenstein phase function $p_{HG}(\theta, g_1)$ [sr^{-1}] with the asymmetry parameter g_1, while $p_{HG}(\theta, -g_2)$ [sr^{-1}] is backward directed phase function

with negative g_2 and scaled by $(1-\alpha)$. Equation 10 refers to the two-term Henyey-Greenstein function (TTHG). We can retrieve the first moment of the TTHG phase function g_{TTHG} from the relationship:

$$g_{TTHG} = \langle \cos\theta \rangle = \alpha(g_1 + g_2) - g_2 \ . \tag{11}$$

A more physics-based phase function derived for sea ice was calculated considering Mie solutions for the spherical air bubbles and the Wentzel-Kramers-Brillouin approximation for non-spherical brine channels (Malinka et al., 2018). In this development, it is assumed that the scattering of other inclusions, e.g., lithogenic, biogenic particulates or solid salt crystals are negligeable. For solid salts, this assumption is reasonable as the temperatures were above -23°C (hydrohalite precipitation temperature) during both sampling days. The derivation steps of the phase function, $p_M(\theta)$, is described in appendix B.

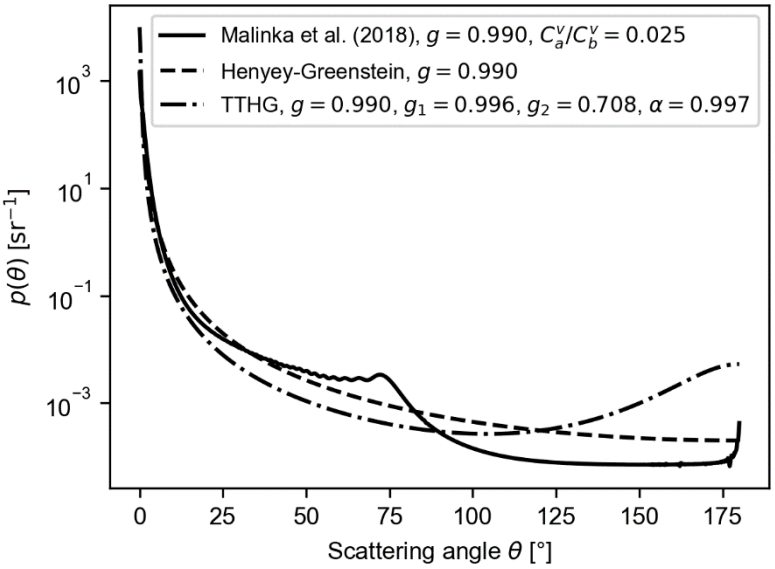

Figure 2: Scattering phase functions $\boldsymbol{p}(\boldsymbol{\theta})$ [sr^{-1}] tested for HydroLight simulations. They are the Henyey-Greenstein (HG), the two-term Henyey-Greestein (TTGH) and the Wentzel–Kramers–Brillouin and Mie computed (Malinka et al., 2018) functions. The three phase functions have the same first moment $\boldsymbol{g}$ = 0.990, while they differ in their second and third moments.

We performed three simulations with identical geometrical conditions (layer numbers and thicknesses), scattering, and absorption coefficients. For each simulation, we used either $p_{HG}(\theta)$, $p_{TTHG}(\theta)$ or $p_M(\theta)$ adjusted to have an average cosine $g \sim 0.99$, a proper value when there are much more brine pockets than bubbles in columnar sea ice (Light et al., 2004; Mobley et al., 1998). With $g_1 = 0.9960$, $g_2 = 0.7083$, and $\alpha = 0.9967$ for the TTHG equation, we obtained a phase function with an asymmetry parameter of $g_{TTHG} = 0.9904$ (see Fig. 2). For the Mie computed phase function, using a ratio of volume concentration air-to-brine of $C_a^v/C_b^v = 0.025$ (see appendix B for more information on the ratio), we obtained a phase function with $g_M = 0.9903$ (see Fig. 2). To verify if the shape of the phase function has an impact on the correspondence between the simulations the measurements, we used the mean unbiased percent difference (*MUPD* [%]) metric:

$$MUPD_i = 200 \cdot \frac{1}{K}\frac{1}{N} \cdot \sum_{k=1}^{K}\sum_{n=1}^{N} \frac{\left[\bar{L}_{i,HL}(z_k,\theta_n) - \bar{L}_{i,Field}(z_k,\theta_n)\right]}{\left[\bar{L}_{i,HL}(z_k,\theta_n) + \bar{L}_{i,Field}(z_k,\theta_n)\right]} \quad (12)$$

and the root-mean-square error (*RMSE* [%]):

$$RMSE_i = 100 \cdot \sqrt{\frac{1}{K}\frac{1}{N} \cdot \sum_{k=1}^{K}\sum_{n=1}^{N} \left[\frac{\bar{L}_{i,HL}(z_k,\theta_n) - \bar{L}_{i,Field}(z_k,\theta_n)}{\bar{L}_{i,HL}(z_k,\theta_n)}\right]^2} \quad (13)$$

with $\bar{L}_{i,HL}(z_k,\theta_n)$ being the HydroLight azimuthally averaged radiance while $\bar{L}_{i,Field}(z_k,\theta_n)$ represents the field measurements at each discrete depth z_k [cm] and θ_n the zenith angles between 0° and 180°. By comparing the metrics obtained after performing the RT simulations with the three different phase functions (TTHG, Malinka, and HG), we will be able evaluate the level of improvement achievable by fine tuning the phase function.

2.6 Inversion errors

Manual inversion, being a basic method, certainly leads to errors when inferring inherent optical parameters. Therefore, we developed an experiment to estimate the error level that percolates through the process. The method consists in using a vertical profile of angular radiance distributions obtained from HydroLight model simulations and then trying to find the inherent optical properties that generated them. Two people were needed for the experiment: one to freely create a set of ice layers (with numbers and sizes at his desire) having constant IOPs (absorption, scattering coefficient and anisotropy parameter g of the Henyey-Greenstein phase function) and the other one (the expert) to perform the fit following the steps described in section 2.4. For a valid inversion error determination, we made sure that the expert had no prior idea of the number of layers, their thicknesses, and their optical properties. The optical properties setter had to select those within range of possible values for sea ice with regards to the typical vertical evolution of the structural-optical properties (surface scattering layer, drained layer, interior ice, etc.), so that the expert could have the same amount of knowledge as if it was real measurements. They also had information about ice total thickness and freeboard, parameters always available as they can be retrieved on field.

First, we assessed the errors from the inversion by itself using perfect angular radiance distributions as outputted directly by HydroLight. Secondly, to check if the discrepancies (*MUPD* [%] and *RMSE* [%]) between the actual radiances measured and simulated could lead to reasonable estimation of the IOPs, we had to examine the errors when adding artificially generated noise to light fields generated from HydroLight. For that purpose, an analysis of the errors between the simulated and measured spectral radiance distributions azimuthally averaged was done in Fourier space using data from AO2018 mission. This enabled us to pinpoint the spectral signature of the error and to generate new ones to add to the HydroLight radiance. In both experiment cases (with and without noise), the ice slab was set to 2.0 m in total with 1.0 m deep water zone directly below. The person setting the IOPs had also the liberty to give optical parameters to the water column within reasonable range.

3 Results

3.1 Field measurements

3.1.1 High Arctic

Figure 3 shows spectral angular radiance distributions as acquired by the camera for the three spectral bands. In the first row (Fig. 3a-c), the spectral components of the geometric light field $\bar{L}(\theta, \phi)$ for the depth of 40 cm are shown while the second row (Fig. 3d-f) displays normalized-radiance distributions vertically stack for depths between 40-160 cm with increments of 40 cm. From these three latter plots, the downward directionality of the radiance field increasing with depth is apparent, with accentuation of the phenomenon at longer wavelengths. The removal (from top to bottom) of the radiation travelling upward ($\theta > 90°$) is larger compared to the removal of photons below 90°. From 20 cm to 200 cm, $\bar{\mu}_d$ varies between 0.521-0.555 at 540 nm and between 0.531-0.562 at 600 nm (see full curves of Fig. 4d). For the upwelling light field, the slopes with vertical positioning inside ice are lager as we observe variations in $\bar{\mu}_u$ from 0.483-0.336 (540 nm) and 0.482-0.333 (600 nm) between 60 cm and the ice-ocean interface (200 cm), respectively. As an average cosine for the upwelling photons of 1.0 represents completely straight-upward light fluxes ($\theta = 180°$), reduction of $\bar{\mu}_u$ with depth suggests that we gradually find less radiation at larger zenith angles. Another apparent optical property, the diffuse attenuation coefficient, gives insights on the presence of different layers in the ice column. Figure 4h shows these coefficients for the downward light field. The bulk diffuse attenuation coefficients for the total ice are 1.35 m^{-1} (480 nm), 1.37 m^{-1} (540 nm), and 1.58 m^{-1} (600 nm). At the top (0-20 cm), the average K_d are 4.29 m^{-1} (480 nm), 4.46 m^{-1} (540 nm), and 5.06 m^{-1} (600 nm). Just below, an intermediate layer sits up to 80 cm, with average values of 1.62 m^{-1}, 1.68 m^{-1}, and 2.04 m^{-1} for the blue, green, and red spectral bands, while between 100-160 cm, these K_d decrease to averages of 0.61 m^{-1}, 0.59 m^{-1}, and 0.69 m^{-1}. Then, the spectral K_d increases in the last centimeters of ice where the interface between the sea and ocean sits (see Fig. 4h).

As mentioned in section 2.4, the planar downward, planar upward and total scalar irradiances helped in fitting the IOPs by matching the measured quantities to the modeled ones. Figure 4a-c present these radiometric quantities. We notice that the simulated irradiances follow relatively well the measured ones. The average relative difference are 10.0, 27.1, and 12.4 % for the planar downwelling, the planar upwelling and the scalar total light fields, respectively. The relative differences spectrally averaged are all below 10 % at depths between 20-160 cm for E_d and E_o, and at depths within 60-160 cm for E_u. Indeed, higher discrepancies are found as we get closer to the upper and lower boundaries. This is especially apparent looking at average cosines ≤ 20.0 cm for the upwelling (Fig. 4e), and total (Fig. 4f) radiance distributions, where surface hole effects seem to have perturbed the measurements (displayed as full lines). Table 1 shows the set of IOP profiles that generated the modeled irradiances. We inverted constant absorption coefficient values for the entire ice column of 0.060, 0.0775, and 0.145 m^{-1} at the 480, 540, and 600 nm bands respectively. The Gershun's law calculated absorption coefficients from Eq. (**5**) are displayed in Fig. 4i for the measured (full lines) and simulated (broken lines) irradiances. We did not isolate unchanging $a(z)$ as a function of depth like the HydroLight inversion. At the top, this again may be due to surface effects that contaminated our

measurements. Also, we inferred negative values for the Gershun's law absorption coefficients caused by an increase of the net irradiances between 80-100 cm. (see Fig. 4g). Nonetheless, we interestingly noticed – by taking the depth median of all the Gershun's law – absorption coefficients of 0.080, 0.075, and 0.137 m^{-1} for the blue, green, and red channels. These coefficients are close to the HydroLight manually fitted values. Table 1 gives the fitted scattering properties, where we clearly observe distinctions between the 20-cm defined layers. Below the surface 20-cm layer having the largest b' of 25.5 m^{-1}, the three subsequent slabs have similar values of 4.8 m^{-1}. The b'drops to 2.4 m^{-1} for the 80-100 cm slab, while two consecutive layers of 40 cm are found below with smaller b' of respectively 1.1 m^{-1} (100-140 cm) and 0.8 m^{-1} (140-180 cm). We also note an increase in scattering in the last layer. Asymmetry coefficients of 0.99 for every layer below 20 cm were found to fit well within the measured irradiances, except at the surface, where a g of 0.85 was found.

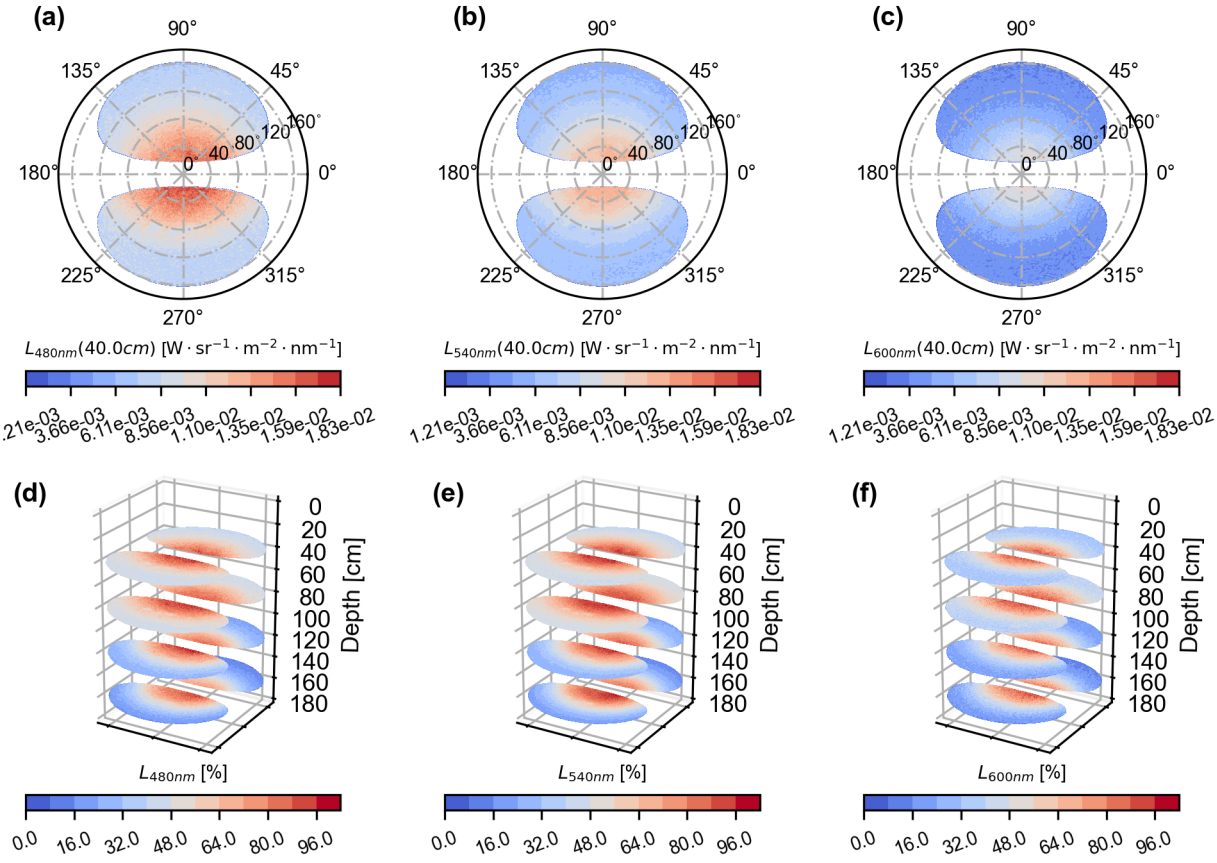

Figure 3: Angular spectral radiance distribution [W sr^{-1} m^{-2} nm^{-1}] as measured by the camera in High Arctic (AO2018 expedition). The top row (a), (b) and (c), displays the light fields at 40 cm depth for the blue, green, and red bands respectively. The zenith coordinates θ corresponds to the radial circular lines while the azimuth φ are the angular lines. The white regions are the missing values over the 4π steradians sphere due to the 76° reduced field of view in water. The second row presents the radiance distributions at various depths (40, 80, 120 and 160 cm), but normalized to their respective maximum.

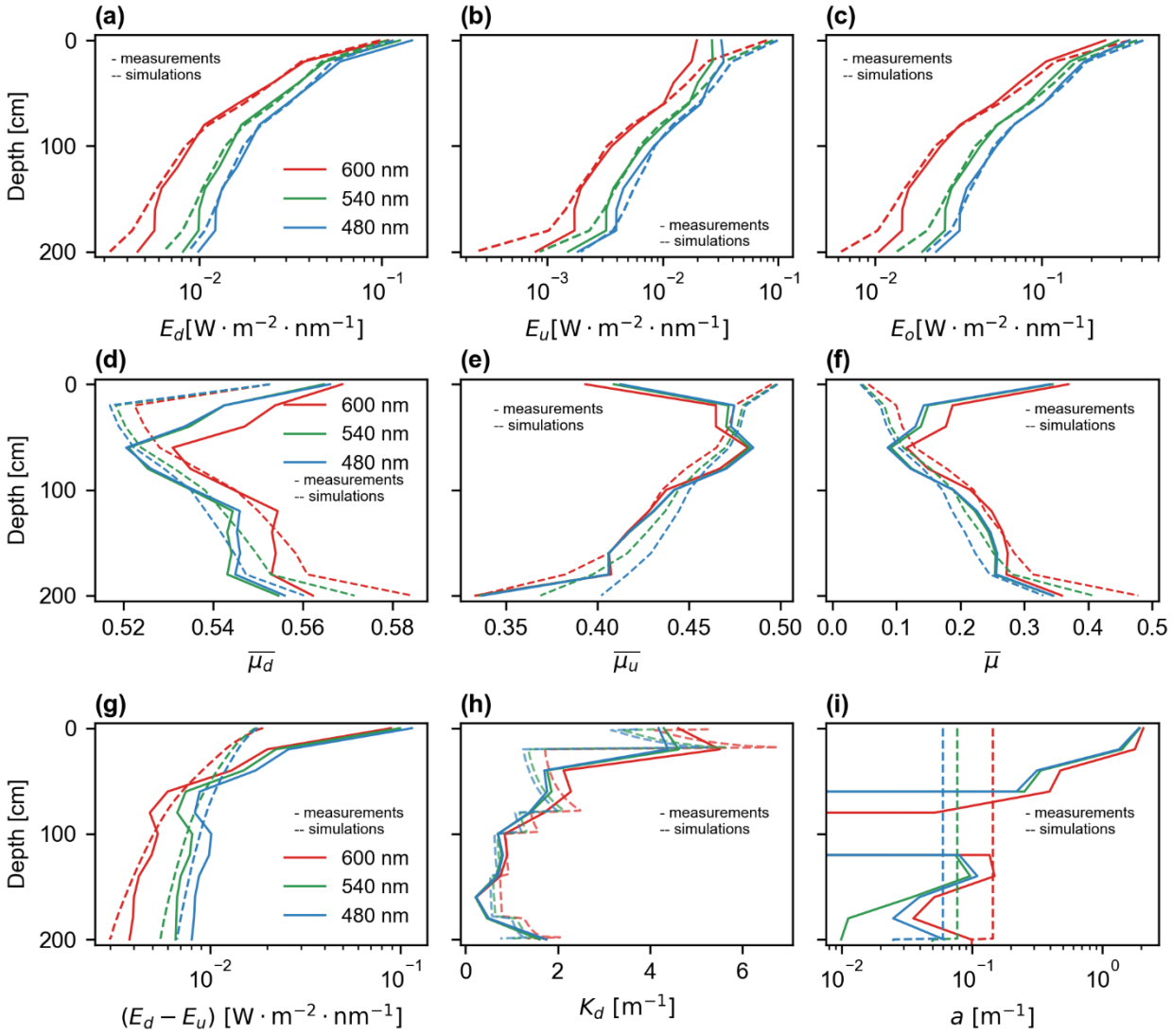

Figure 4: Vertical profiles of planar downward irradiance (a), upward planar irradiance (b), and scalar irradiance (c). The second row shows the average cosines for respectively (from left to right) the downward, the upward, and the complete radiance values angularly defined. In the last row, we see the net irradiance as a function of the depth in sea ice (g), the diffuse attenuation coefficient for the downwelling irradiance, $\boldsymbol{K_d}$ (in $\mathrm{m^{-1}}$), (h), and the Gershun's Law derived absorption coefficient (i). For each subfigure, the three spectral band curves are displayed according to their colour. The solid lines are the measurement results, while the broken ones are the RT simulation outputs.

The first row of Fig. 5 shows azimuthally averaged radiance measured and modeled at multiple depths inside sea ice. Distributions at the surface are not shown as they were too much affected by hole effects and operator shadow. The angular radiance distributions are also not displayed at 180 cm and 200 cm depths because of uncertain camera vertical positioning.

The left to right columns (Fig. 5a, b, c) correspond respectively to the 480, 540 and 600 nm spectral bands. The average errors, given from Eq. (12) for the *MUPD* and Eq. (13) for the *RMSE*, are respectively 4.63 % and 10.00 % (blue channel), 1.86 % and 9.29 % (green channel), and 1.81 % and 12.91 % (red channel). At depths ≤ 60 cm, there are important differences between the measured and simulated angular radiance distributions near both angular extremities (20˚ and 160˚). As we progress deeper inside the ice slab, these extremities errors seem to reduce as does the error curves at all zenith angles compared to their lower depth counterpart.

Table 1. Inherent optical properties (IOPs) inverted from HydroLight and depth resolved angular radiance distributions measured in High Arctic (AO2018 expedition). The absorption coefficients a [m^{-1}], the scattering coefficients b [m^{-1}], the anisotropy coefficient of the phase function g, the reduced scattering coefficient $b(1-g)$ are given for the ice splitted into slabs of 20 cm between 0 – 200 cm. The dimensionless similarity parameters S combining all the IOPs, calculated from Eq. (6), are also given.

Layers	Depths [cm]	High Arctic								
		a [m^{-1}]			*b* [m^{-1}]	*g*	*b (1-g)* [m^{-1}]	*S*		
		480 nm	540 nm	600 nm				480 nm	540 nm	600 nm
SSL	0 – 20	0.060	0.0775	0.145	170	0.85	25.5	0.0485	0.0550	0.0752
OII	20 – 40	0.060	0.0775	0.145	480	0.99	4.8	0.1111	0.1261	0.1712
OII	40 – 60	0.060	0.0775	0.145	480	0.99	4.8	0.1111	0.1261	0.1712
OII	60 – 80	0.060	0.0775	0.145	480	0.99	4.8	0.1111	0.1261	0.1712
OII	80 – 100	0.060	0.0775	0.145	240	0.99	2.4	0.1562	0.1769	0.2387
YII	100 – 120	0.060	0.0775	0.145	110	0.99	1.1	0.2274	0.2565	0.3413
YII	120 – 140	0.060	0.0775	0.145	110	0.99	1.1	0.2274	0.2565	0.3413
YII	140 – 160	0.060	0.0775	0.145	80	0.99	0.8	0.2641	0.2971	0.3917
YII	160 – 180	0.060	0.0775	0.145	80	0.99	0.8	0.2641	0.2971	0.3917
SL	180 – 200	0.060	0.0775	0.145	150	0.99	1.5	0.1961	0.2216	0.2969

3.1.2 Chaleur Bay

One of the vertical profiles of spectral radiance captured at Chaleur Bay is displayed in the second row of Fig. 5. At that location the ice was 80 cm thick with a freeboard of 18 cm. We show only the zenithal light field below the freeboard as the other measurements were significantly affected by the light reaching down the hole. Radiances obtained with HydroLight RT simulations using the retrieved inherent optical properties (see section 2.4 for the procedure) are presented in Fig. 5d, e, and f as plain lines for each measured depth. The IOPs inferred are given in Table 2 for equally thick layers of 20 cm each (in-ice). We inverted a higher scattering surface layer with a b' of 37.5 m^{-1}, two subsequent regions (20-40 cm, 40-60 cm) of

intermediate scattering level with $b' = 6.4$ m^{-1} and $b' = 7.2$ m^{-1}, and a last layer (before the water column) with a reduced scattering coefficient of 2.8 m^{-1}. This latter coefficient is slightly smaller than for the other layers, but still represents a large value compared to what was observed in High Arctic interior ice. For all the in-ice layers except at surface having a g of 0.85, an asymmetry coefficient of 0.99 was inferred for the Henyey-Greenstein phase functions.

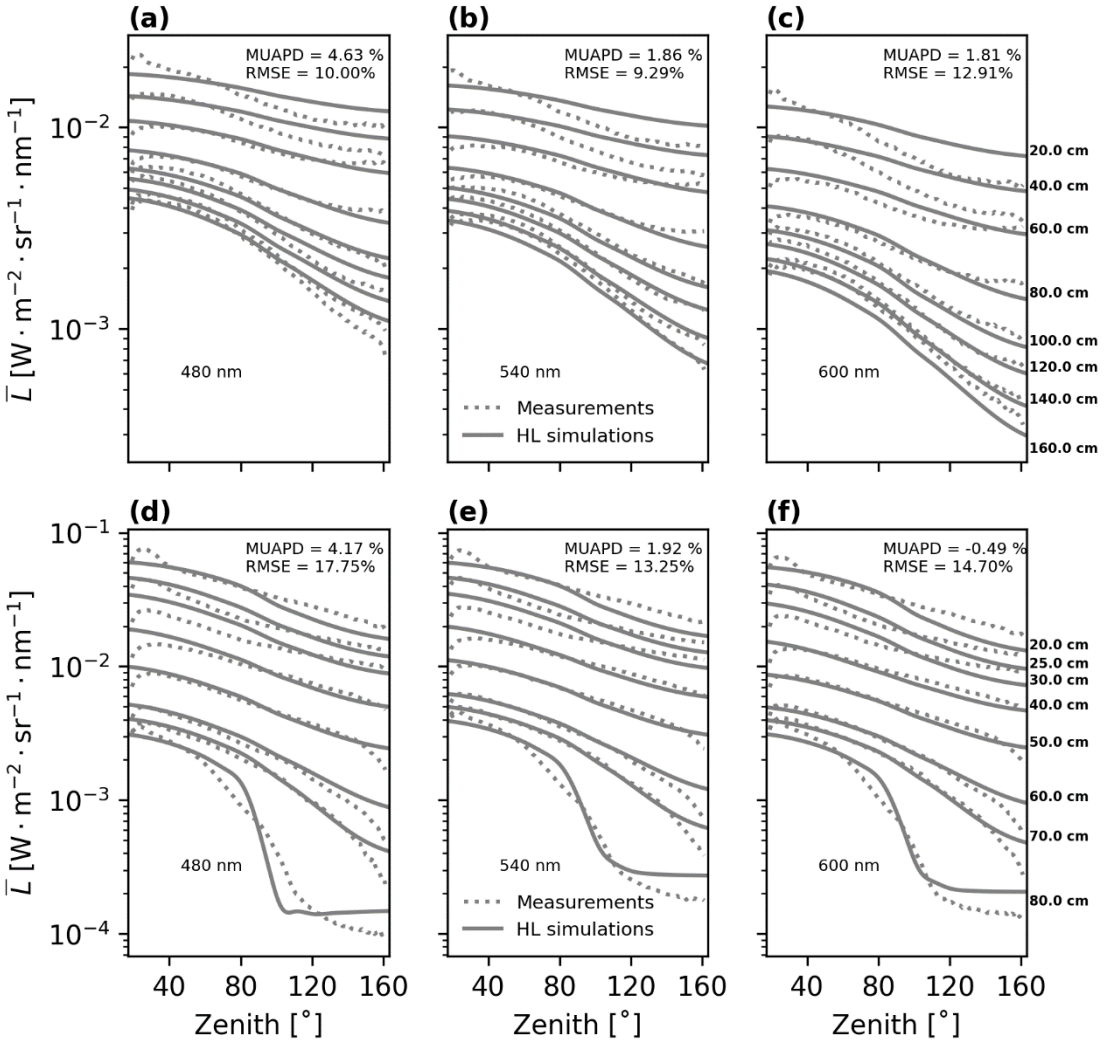

Figure 5: Depth resolved spectral angular radiance distributions azimuthally averaged. The first row represents the High Arctic radiance for the (a) 480, (b) the 540, and (c) the 600 nm spectral channels, while the second row shows the same bands (in order from left to right) but for the Chaleur Bay site. The broken lines are the camera measurements and the full lines are the radiance data modeled with HydroLight (both at 1° angular resolution).

In addition to large in-ice scattering coefficients at Chaleur Bay site, we also obtained high absorption coefficients in each channel. The absorption coefficients for the blue band are larger than for the green channel for most of the depths as well as

being larger than the red band for all layers except those at 0-20 cm and 60-80 cm. The high absorption of the medium is also reflected in the K_d coefficients which are higher than those of arctic sea ice. The diffuse planar downwelling attenuation coefficients are shown in the supplemental document (Fig. S1) along with all the same quantities as the ones presented in Fig 4. The agreement between the RT simulated and measured zenithal radiances, quantified using the *MUPD*, are of 7.92, 0.87, and 6.34 % respectively for the 480, 540, and 600 nm channels. For the root-mean square errors, which gives a better idea of the residuals, we obtained 16.04, 14.22, and 16.10 % for the same spectral bands. These large discrepancies (larger than for the High Arctic inversion) may be caused by more impact of hole and self-shading on the measurements. Indeed, as seen in the second row of Fig. 5, the errors are greater at the FOV limits (at low and large zenithal angles); image regions prone to the impacts of the drilling hole and the shading of the stick we inserted in it.

Table 2. Ice inherent optical properties obtained by fitting internal measurements of radiance at Chaleur Bay site (on 23 March 2022) with HydoLight radiative transfer simulations. We provide the absorption coefficients a [m^{-1}], the scattering coefficients b [m^{-1}], the anisotropy coefficient of the phase function g, the reduced scattering coefficient $b(1-g)$ as well as the similarity parameter S for 20 cm equal layers.

Layers	Depths [cm]	Chaleur Bay								
		a [m^{-1}]			*b* [m^{-1}]	*g*	*b (1-g)* [m^{-1}]	*S*		
		480 nm	540 nm	600 nm				480 nm	540 nm	600 nm
SSL	0 – 20	0.30	0.30	0.30	250	0.85	37.5	0.0891	0.0891	0.0891
II	20 – 40	1.40	1.30	1.75	640	0.99	6.4	0.4237	0.4109	0.4634
II	40 – 60	1.40	1.10	1.00	720	0.99	7.2	0.4035	0.3640	0.3492
II	60 – 80	0.40	0.30	0.30	280	0.99	2.8	0.3536	0.3111	0.3111

3.2 Impact of the phase function shape

We ran HydroLight RT simulations multiple times with given sets of inherent optical properties, while using alternatively for each the three different depth-constant phase functions shown in Fig. 2. The RT computed radiances using the Henyey-Greenstein (HG), the two-terms Henyey-Greenstein (TTHG), the Malinka et al. (2018) phase functions are compared to the field measurements with statistical metrics (*RSME* and *MUPD*) given in Table 3. Between the function computed from Mie equations and the Henyey-Greenstein functions, the resulting discrepancies are negligeable. There are only 0.1 % differences for the *RMSE* at 540 nm and the *MUPD* at 480 nm. As for the two-term Henyey-Greenstein function, the metrics decreased more noticeably from its one-term counterpart. There were decreases ranging between 0.4 %-1.7 % for the *RMSE* and reaching

a maximum of 1.3 % for the *MUPD*. Still, the changes in the metrics are all relatively small from one phase function to another, which shows that their shape has limited impact on the angular radiance distributions.

Table 3. Statistical descriptors of differences between simulated (HydroLight RT) and field observed zenithal angular radiance distributions. Three different depth constant phase functions were tested in HydroLight: Henyey-Greenstein (HG), two-terms Henyey-Greenstein (TTHG), and Malinka et al. (2018) functions. The root-mean-square errors (*RMSE*) and the mean unbiased percent differences (*MUPD*) are given for every spectral bands.

Phase functions	*RMSE* [%]			*MUPD* [%]		
	480 nm	540 nm	600 nm	480 nm	540 nm	600 nm
HG	10.0	9.3	12.9	4.6	1.9	1.8
TTHG	9.6	8.1	11.2	3.4	0.6	1.8
Malinka et al. (2018)	10.0	9.2	12.9	4.7	1.9	1.9

3.3 Inversion errors

We generated two sets of artificial in-ice angular radiance distributions from realistic depth dependent IOPs (unknown to the fitting expert) and evaluated the inversion errors of the procedure exposed in section 2.4. We did a first case with vertical stack of five in-ice layers with different IOPs over a total thickness of 2.0 m. We created a second scenario with four layers over a 2.0 m deep ice as well as errors addition to radiance distributions (*RMSE* of 13.60 % spectrally averaged). In both cases, a single layer water column of 1.0 m was added below ice. The results are presented in Fig. 6, in which the two rows show respectively the IOPs of first and second scenario. Focusing on the first case, we observe discrepancies between the true and inverted IOPs below 20 %. Inversion of absolute coefficients (Fig. 6a-b) appears more challenging than the three other quantities. The depth averaged errors are between 9.6-19.4 % for the absorption coefficients and 12.5 % for the scattering coefficients. As we got good agreements for the asymmetry parameter g (error of 0.2 %), we notice slightly lower divergences for the reduced scattering coefficient of 11.3 % compared to its absolute counterpart. This is also observed for the second case which has an even larger error on b (64.3 % as displayed on Fig. 6g), but because of low-level error on the parameter g, we ultimately get an effective error on b' of only 17.2 % (Fig. 6i). The similarity parameters also are less affected by the inversion methodology. We are ultimately fitting the S parameter implying that if we miss the absorption coefficients inversion, it gets compensated by better inversion of the reduced scattering coefficients. This is observed for both scenarios (see Fig. 6e and 6j) with, as expected, larger errors for the case with noise addition. However, even with a *RMSE* of 13.60 % between the original radiance and the erroneous ones, the expert was able to retrieve the similarity parameter within 25 %. Another observation, without prior knowledge on the number of sea ice layers, the expert was able to estimate with precision their amounts, i.e five and four layers for the two scenarios respectively. This is also true for an inversion case created with a total number of 13 layers for the ice, the latter shown in the supplemental document (see Fig. S2).

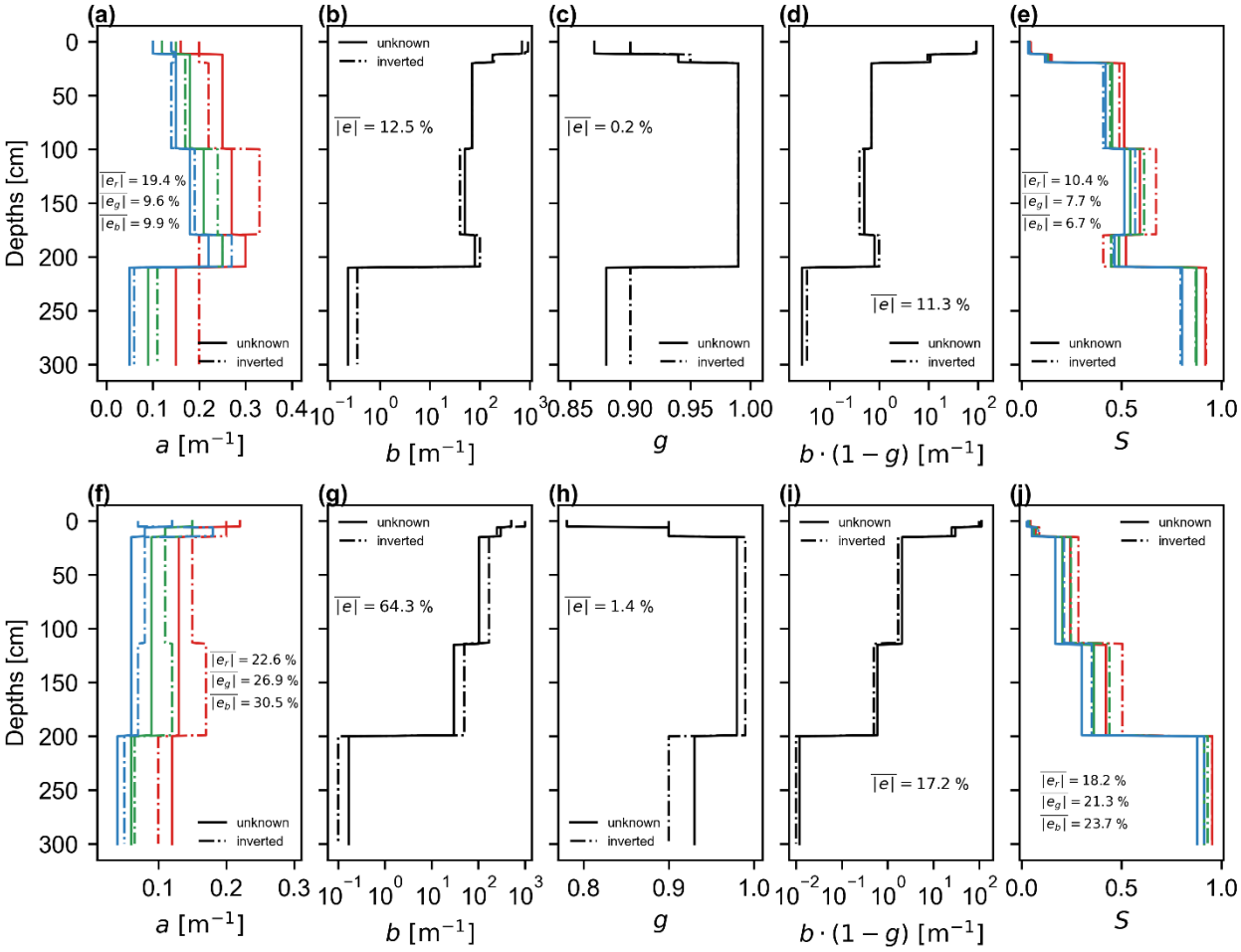

Figure 6: Inherent optical properties (IOPs) inversion error estimations. The first row shows the true unknown (full lines) and fitted (broken lines) vertical profiles of IOPs. Those inherent optical properties are the spectral absorption coefficients (a), the scattering coefficients (b), the asymmetry parameters of the phase function (c), the reduced scattering coefficients (d), and the similarity parameters (e). The row just below displays the inversion error results, but for another set of IOPs and after addition of noise/offset to the simulated radiance distributions generated by HydroLight. In each figure, the average errors considering the part related to internal ice slab (200.0 cm thick for both cases) are given.

4 Discussion

4.1 Field measurements

In MY ice of the High Arctic site, depth-constant absorption coefficients of 0.060 (480 nm), 0.0775 (540 nm), and 0.145 m^{-1} (600 nm) properly fitted the radiometric measurements in each band. These are slightly higher than the absorption coefficients reported for pure bubble-free ice by Grenfell and Perovich (1981) of 0.043, 0.0683, and 0.12 m^{-1} at respectively 480, 540, and 600 nm. For the absorption coefficients derived through Gershun's law (Fig. 4i), we notice larger surface values which seems wrong as the presence of bubbles in these layers (SSL and DL) should slightly reduce the absorption coefficient, a. We think

that this may be due to hole effects, a bright one at the surface, increasing downwelling irradiance and a dark spot down under decreasing the upwelling irradiance. There are also possible absorption enhancement effects happening in strongly scattering layers (Ehn and Mundy, 2013) and particulate absorbers that might have been part of the ice surface structure. The Gershun's law depth median absorption coefficients are of 0.080, 0.075, and 0.137 m^{-1} for respectively the 480, 540, and 600 nm channels. The larger median coefficient in the blue compared to the green spectral band may be surprising but agrees with previously reported values found in landfast sea ice (Ehn et al., 2008b). In fact, over the region of negative absorption coefficients (80-100 cm), we notice larger a in the green band compared to the 480 nm channel, while for depths > 100 cm, the blue absorption coefficients surpass those in the green (see Fig. 4i). This is apparent also in the color of the ice of Fig. 7b – extracted from jpeg images saved along the raw ones – which displays bluer colors becoming greener at 100 cm. The increase of a for shorter wavelength could be caused by algal or non-algal particulates that may be larger in concentrations as we progress toward the ice-ocean interface (Ehn et al., 2008b). Regarding the negatives inverted absorption coefficients caused by the increase in net irradiance (see Fig. 4g), we believe that measurements artefacts may be responsible. They include possible angular misalignment of the optics inside the hole, surface effects such as shadow of the operator near the hole or snow displacement. The average cosine $\bar{\mu}$ has the same spectral trends as the measured absorption coefficients being related through the Gershun's law presented in Eq. (**5**). The increase of $\bar{\mu}$ with depth starting from 60 cm (see Fig. 4f) reflects higher proportion of light rays that vanished at large angles the deeper we are in ice. This is explained by being closer to the ice-ocean interface where there are less photons going upward due to the significantly less scattering in the last ice layers and in the ocean. This is also why the gradient with depth for $\bar{\mu}_u$ is larger than $\bar{\mu}_d$, as the light rays in the downwelling field are less affected by the proximity of the ice-ocean interface. No in-ice average cosine measurements were found in the literature, but some reported $\bar{\mu}_d$ just below sea ice bottom ranging from 0.59 to 0.70 based on direct observations (Katlein et al., 2014; Massicotte et al., 2018; Matthes et al., 2019) or models (Arrigo et al., 1991; Ehn and Mundy, 2013). Downwelling average cosines measured by Matthes et al. (2019) show spectral $\bar{\mu}_d \leq 0.59$, 3.0 m below bottom for an ice covered with snow. This makes our observations at 200 cm of 0.556, 0.555, and 0.562 for respectively the 480, 540, and 600 nm bands plausible.

The scattering coefficients of the site in the Arctic were assumed spectrally invariant, a correct simplification in Mie regime when the scatterers are large and distant as diffraction and interference effects are negligible (Grenfell, 1983). Although we set equal 20 cm thicknesses for all the slabs of the simulated ice column (see Table 1), it is interesting to note that subsequent layers merged into larger regions of constant scattering properties, which reveals zones of homogeneous microstructure. The first 20 cm slab includes the SSL, measured on site at 10 cm, and has the highest reduced scattering coefficient, $b' = 25.5$ m^{-1}, because of its structure as a porous mixture of ice crystals and air. That b' is in the range of previous value inverted for MY ice SLL, between 20-150 m^{-1} (Light et al., 2008). Just below, normally sit the DL constrained by the freeboard position. This layer is also known to cause significant scattering as the inclusions are drained and the ice more porous (Light et al., 2008). As the freeboard was measured at a depth of 17 cm, the first 20 cm layer optical depth has contributions from both the surface scattering layer and 7 cm of drained layer. The four subsequent slabs (20-100 cm) below freeboard have also considerable

inverted b' of 4.8 m^{-1} and 2.4 m^{-1}. These values are larger than those inferred for MY interior ice during summer of 1998 in the Beaufort Sea, which range between 0.5-1.8 m^{-1} (Light et al., 2008). They however fall in the gaps of larger b' of 2.1-4.4 m^{-1} (between 6-76 cm) and 2.8-7.1 m^{-1} (between 10-100 cm) measured respectively inside snow covered and bare first-year interior ice (Perron et al., 2021). Below 100 cm, we observed b' inside the Light et al. (2008) II interval as our values are within 0.8-1.5 m^{-1}. This leads us to assume that the ice at that High Arctic site was probably composed of two types of more translucent interior ice; an old II (OII) from 20-100 cm and a younger II (YII) from 100-200 cm. MY ice is known to have large variations in its optical properties and the in boundaries of its different layers due to multiple melt and growth episodes (Pegau and Zaneveld, 2000). This likely means that the YII was recently formed, while the OII layer was interior ice shaped during previous winters, giving time for brine pockets to be drained over multiple melt seasons (Perovich et al., 2002). Higher scattering in the upper half of the ice column was also evident in optical observations and x-y investigations conducted a few hundred meters away on the same ice floe (Katlein et al., 2021). From this last study, a four-layer model using DORT 2002 RT model (Edström, 2005) helped inverting reduced scattering coefficients of 25 m^{-1} for the surface scattering layer and 2.5 m^{-1} for the interior ice. This is very close to our inference of 25.5 m^{-1} for the SSL and falls near the center value of 2.8 m^{-1} of our range for the interior ice (0.8 m^{-1}-4.8 m^{-1}). In the last ice layer (180-200 cm), we notice an increase of the scattering coefficient that coincide with the skeletal layers at the ice-ocean interface. Below 20 cm, the Henyey-Greenstein phase function has a given depth constant high asymmetry parameter g of 0.99 (highly forward peaked scattering) that is in accordance with previous works on radiative transfer inside sea ice (Mobley et al., 1998; Light et al., 2004; Petrich et al., 2012; Ehn et al., 2008b; Maffione et al., 1998). At the surface, we set the g to 0.85 from the literature (Light et al., 2004) as previous Mie calculations give an asymmetry parameter in that vicinity from larger volume fraction of air bubbles in the layer.

At the Chaleur Bay site (80 cm ice thickness), non-constant absorption coefficients with depth permitted better agreements between the simulations and the radiometric observations. The ice color for each depth displays in Fig. 7c also supports variation of the coefficients with depth as the RGB vary greatly depending on position within the slab. The spectral a inferred are between 0.30 m^{-1} and 1.75 m^{-1} in the ice slab. Above water (the first 20 cm layer), we notice smaller absorption coefficients (0.30 m^{-1} for each band) compared to the rest of the ice column that may be caused by drained brine pocket over the 18 cm freeboard. This layer is porous and makes up a non-negligible part of the first 20 cm simulated slab. Directly below, we observe a significant increase of the coefficients up to 1.40, 1.30, and 1.75 m^{-1} for the 480, 540, and 600 nm spectral channels respectively. Although being quite large, we think that these values are plausible as the site is situated near the shore and close to villages with industrial activities. Thus, particulate matter of natural or anthropogenic origins (from air or water) could have accumulated in the ice during its different stages of formation and aging. It is likely also that algal particles could have been present inside the medium, which would also explain larger absorption in the lower part of the visible spectrum. Absorption coefficient over 1.0 m^{-1} were inverted previously for sea ice in Liaodong Bay, which is surrounded by many industrial, agricultural, and residential zones (Xu et al., 2012b). Obviously, further investigation would be necessary to confirm those assumptions. The 40-60 cm layer also has large a, but slightly lower in the 540 nm and 600 nm bands (these remain stable in

the blue), while we observe a drop in the 60-80 cm layer. Obviously, the inferred coefficients could be affected by boundary and absorption enhancement effects. Higher absorption coefficients in the blue band compared to the green channel (see Table 2) make sense when looking at Fig. 7c as we notice greener colors in comparison to those in High Arctic (Fig. 7b). For the scattering, the first layer which includes the snow cover, the SSL, and the DL, has the largest reduced coefficients b' which is in the same range of what was observed in the Arctic. The two subsequent slabs (20-60 cm) have lower b' values of 6.4 m^{-1} and 7.2 m^{-1} respectively, but still slightly higher than past observations in interior ice (and those presented in this work in High Arctic). From our discussions with a local ice fisherman, we understood that heavy and multiple snowfalls during winter had come to melt and refreeze, forming layers of coarse ice grains. These are superimposed ice layers (Ehn et al., 2008b) and would explain the larger scattering coefficients inverted in the zones below freeboard.

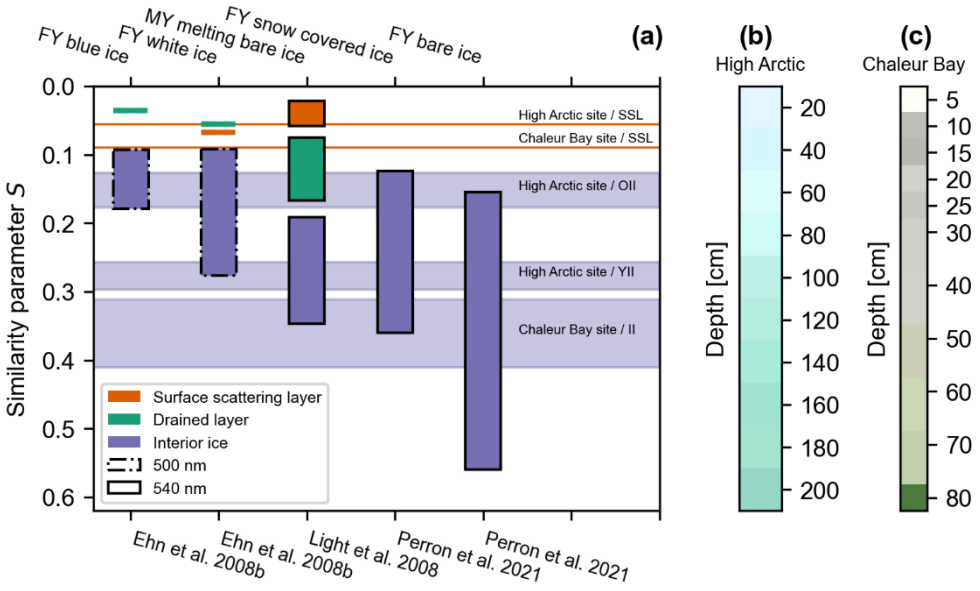

Figure 7: (a) Summary of the similarity parameter ***S*** inverted from measurements at both High Arctic and Chaleur Bay sites, and those reported in previous studies for different types of sea ice. The vertical bars represent the past measurements (Ehn et al., 2008b; Light et al., 2008; Perron et al., 2021) and the background horizontal lines are the range of our values. To calculate the similarity parameters of Light et al. (2008) and Perron et al. (2021), we used the absorption coefficient of pure ice at 540 nm (Grenfell and Perovich, 1981). The ***S*** of Ehn et al. (2008) are provided in their paper at 500 nm. (b)-(c) RGB color of the High Arctic and Chaleur Bay ice respectively extracted from jpeg images saved along DNG files (see Fig. S4 in the supplemental document for some of the rectilinear images). Obtaining these two 1D images involved: 1) taking the average pixel value inside a square at the center of the image, 2) normalization by the diffuse planar downwelling attenuation coefficient spectrally averaged, 3) normalization by the maximum.

For highly scattering media such as the ice of the studied sites, the inverted IOPs are only true under the similarity principle as two different sets of IOPs with the same S give similar light fields. Following Eq. (6), if the ratio b'/a increases, the similarity parameter decreases. Figure 7a presents the ranges of inferred similarity parameters for the High Arctic and the

Chaleur Bay fieldworks (background shaded regions) as well as some literature values for comparisons. For the High Arctic (depth constant absorption coefficients), the reduced scattering coefficients decline as we progress deeper inside the ice which effectively increases S from the top SSL to the internal ice. In Chaleur Bay, it is the inverse situation as the absorption coefficient decrease with depth. Comparing the two sites, we observe higher similarity parameters in the Chaleur Bay FY landfast ice for the SSL and the II due to their greater absorption coefficients. Still, ranging between 0.3111-0.4109 at 540 nm, Chaleur Bay interior ice layer S are within observations made inside FY bare ice (0.1543-0.5593) at Qikiqtarjuaq (Perron et al., 2021). The similarity parameter of 0.3640 in the second to last layer (40-60 cm, see Table 2) is near the higher bounds of both Perron et al. (2021) snow covered FY interior ice and Light et al. (2008) MY bare interior ice having S of 0.3596 and 0.3467 respectively. However, these latter values are caused by small b' while they are due to a larger a for the Chaleur Bay. In High Arctic interior ice, the S for the YII range between 0.2565-0.2971 and have similar values than those observed in melting MY interior ice in Beaufort Sea during summer of 1998 (0.1912-0.3467) (Light et al., 2008). For the OII, the similarity parameters come close to S of interior ice measured in landfast FY ice (Ehn et al., 2008b) and in the drained layer of Beaufort Sea ice (Light et al., 2008). This further support the naming this layer old interior ice. The similarity parameters of the first layer for both sites fall in the range of reported values for the SSL and DL as they include these two layers within 20 cm. For instance, at 540 nm in High Arctic, the S is of 0.055 is close to the one inferred in FY landfast white ice drained layer of 0.0548 (Ehn et al., 2008b), and to the upper bound of 0.0583 for the observed S in the melting MY bare ice SSL (Light et al., 2008).

4.2 Impact of the phase function shape

In sea ice, each layer that sits above and below the current layer act as radiance sources. In this case, the radiance angular distribution at a certain depth is driven by the fact that the sources above are way brighter than those below. There are only few photons coming from very large zenithal angles as the ocean is dark compared to the upper boundary. The angular shape of radiance being driven by the irradiance gradient, only the first moment of the phase function is worthy of our attention. Changing the other moments of the phase function in the simulations did not provide a significant reduction of the errors between the measured and simulated radiance. Also explained by Jacques (2013), the zenithal dependence of the scattering determined by the phase function gets averaged out to $g = \langle \cos\theta \rangle$ due to multiple collisions between the photons and the scatterers. We will observe the same radiance distributions from different phase functions with the same g. The diffusion regime (asymptotic regime) is reached at a depth of one mean free path, $MFP' = 1/(a + b')$ [m], inside the medium (Jacques and Pogue, 2008). In the SSL, we are in that region for High Arctic measurements after only 3.9 cm (see first layer b' of Table 1). Obviously, in some cases where the ice would have small scattering values, we would potentially find traces of the phase function in the angular radiance distributions.

4.3 Errors analysis

Certain sources of uncertainties may have affected the IOPs inversion from the set of measurements presented in this study. These included uncertainties due to the measuring device and its manipulation on-field, source of errors due to the ice structure itself, and HydroLight inversion uncertainties. First, the absolute calibration of the radiance camera bears uncertainties, discussed in details in Larouche et al. (n.d. in prep). Second, potential manipulation errors that could have occurred during fieldwork are the following: misalignment of the optics inside of the hole leading to misaligned angular coordinates of the radiance values, shadow of the manipulators affecting surface measurements, and unprecise depth knowledge as sometimes the holding stick came up folded. Another error affecting the geometric light field is self-shadowing of the camera-stick assembly. We did a brief investigation of self-shading effects which reveals that radiance distributions are affected more strongly at small and large zenithal angles. This likely explains why the simulated and measured angular radiance distributions are more distant at the two extremities of the curves as seen in Fig. 5. In addition, the solid structure of the ice leaves no choice but to dig a hole for internal measurements. From above or below the camera position, the holes create path for light to easily propagate and add to the fluxes that there would be without the opening. These hole effects increase when the camera is positioned near the boundaries, as the hole is seen inside a larger portion of the FOV. A second source of errors due to ice itself is the large spatial variation in its structure (micro and macro scale) over only a few meters (Pegau and Zaneveld, 2000; Frey et al., 2011; Perovich and Gow, 1996). The light field from a nearby region can affect the radiance at the position of interest. This is difficult to discern from our radiance measurements and cannot be simulated in HydroLight. Finally, there is also the anisotropic scattering coefficient that was neglected in this study – as not configurable in HydroLight RT model – and which might have permitted better IOPs inversion and fitting of the field observations.

The inversion method also leaves errors on the IOPs inferred as shown in section 3.3. The problem being underdetermined, we have demonstrated that inferring the right absorption and scattering coefficients is challenging. From perfect simulated irradiances, we obtained a depth averaged error on b of 12.5 %, while from the irradiances with artificial error, a discrepancy of 64.3 %. This error decreases for the reduced scattering coefficient as the expert closely approximated phase function asymmetry parameters. We think that knowing that the sea ice observed phase function first moment are almost always highly forward peaked ($g \geq 0.85$) and having access to both E_d and E_u greatly help in getting the g right and, at the same time, better agreements for the b'. Still, because of the highly scattering nature of sea ice, two combinations of a and b' would give rise to the same light fluxes, which is why we are at the best fitting S. We indeed obtained the lowest inversion errors for the similarity parameter of both perfect and erroneous irradiances cases as seen in Fig. 6.

On the relevance of angular radiance distribution measurements, it has been determined that we could successfully invert the IOPs having simultaneous measurements of E_d, E_u, and E_o. Ultimately, by making the observed and simulated irradiances match, we noticed correspondences when verifying radiances distributions. This is characteristic of the diffusion regime where

the zenithal radiances approach an asymptotic shape decaying with depth at the same rate as the irradiances (Preisendorfer, 1958). The usefulness of radiance over almost 4π steradians resides in that we can collect all of the possible irradiance quantities (E_d, E_u, E_d^o, E_u^o, and E_o) simultaneously from one capture of the 360-degree camera. To gather all of these quantities from currently available radiometers at the same time would be a complicated task as they are usually designed to measure only one type of irradiance. Packaging this into a single profiler would require large assemblies of tens of centimeters. In addition, as we would capture radiance closer to boundaries with non-isotropic incident light field, in layers with small scattering coefficients, the azimuthal and zenithal angular shape of the light field would be of great interest. These conditions could happen in marine environment, for instance inside blue ice of glacier crevasses and icebergs (Warren et al., 2019).

5 Summary

In this paper, we successfully demonstrate the utility of 360-degree cameras to study in-ice radiative transfer. Those compact optical systems enable capture of full radiance angular distributions at fixed point in space and inside three spectral bands (480, 540, and 600 nm). Subsequently, from these distributions, we were able to manually constrain profiles of IOPs by fitting HydroLight simulated radiometric quantities to those measured at two sites: in High Arctic and Chaleur Bay (Quebec). In the two meter thick High Arctic MY ice, we inferred reduced scattering coefficient of 25.5 m^{-1} at the surface, and what it looks like two distinct regions of interior ice: older interior ice (OII) with b' between 2.4-4.8 m^{-1} and younger interior ice (YII) with b' within 0.8-1.1 m^{-1}. Inside the seasonal Chaleur Bay ice, significantly higher light attenuation was assessed, due to both larger absorption, 0.30-1.75 m^{-1}, and reduced scattering coefficients, 2.8-37.5 m^{-1}, compared to the High Arctic site. Presence of superimposed ice as well as absorbing particles (AP and NAP) is thought to be responsible for those observations. Obviously, the inversion problem is greatly underdetermined. From an inversion experiment using HydroLight generated light fields with additional artificially generated errors, we found averaged inversion errors between 22.6-30.5 % for the absorption coefficient and of 64.3 % for the scattering coefficients. In optically thick medium and far from the boundaries, the similarity parameter encompasses all the IOPs and better describe the degeneracy of the AOPs. For that reason, lower inversion errors were retrieved for the similarity parameter with values below 23.7 %. Here are the principal takeaway points prevailing far from boundaries in optically thick medium leading to the asymptotic regime:

- Radiance angular distributions are not more informative for IOPs retrieval than the irradiance quantities.
- The 360-degree camera enables simultaneous measurements of all irradiances (E_d, E_u, E_d^o, E_u^o, and E_o).
- Only the first moment of the scattering phase function (average cosine or asymmetry parameter) has importance.

Much more effort continues to be required in order to improve the inversion methodology. We intend, for future fieldwork, to use independent measurements of absorption coefficients (total, algal and non-algal particulate matters) from melted co-localized sea ice layers as well as *in situ* measurements of b' with a diffuse reflectance probe (Perron et al., 2021). Measurements of ice core temperature, salinity, and birefringence image of the crystals will also be captured. This would give

us insight regarding our inversion strategy and a more complete story of the sea ice IOPs. Better assessments of separated a, b, g will then be possible.

Appendix A

Legendre polynomials form a set of infinite orthogonal functions with interesting mathematical properties. They were previously used to fit angular radiance distributions (Kattawar, 1975). These polynomials are also employed for discretization of radiance in the numerical discrete-ordinate solution for the radiative transfer equation (Stamnes et al., 1988). They were naturally selected for the extrapolation of the unknown radiance values in water (camera below ice freeboard). The spectral radiance $\bar{L}$ [W sr^{-1} m^{-2} nm^{-1}] at a given depth and wavelength is expressed as

$$\bar{L}(\mu) = c_0 + \sum_{l=1}^{l=5} c_l \cdot P_l(\mu)$$

$$P_l(\mu) = \begin{cases} \mu, & l = 1 \\ \frac{1}{2}(3\mu^2 - 1), & l = 2 \\ \frac{1}{2}(5\mu^3 - 3\mu), & l = 3 \\ \frac{1}{8}(35\mu^4 - 30\mu^2 + 3), & l = 4 \\ \frac{1}{8}(63\mu^5 - 70\mu^3 + 15\mu), & l = 5 \end{cases} \quad \text{(A1)}$$

with $\mu = \cos\theta$, P_l and c_l being respectively the Legendre polynomials and their corresponding coefficient of degree l. A least-square minimization routine led to the determination of the Legendre coefficients for the azimuthally averaged spectral radiance. This is possible knowing that azimuthal dependence of the light field under optically thick ice is negligeable (Pegau and Zaneveld, 2000). Angles below 25° ($\mu > 0.906$) were discarded to mitigate the effect of self-shadow and the drastic light fall-off at the edge of the FOV. We used the development of the polynomials up to a fifth degree l, found sufficient to fit different shapes of $\bar{L}(\mu)$ commonly found in the medium. Figure S3 of the supplemental document shows some results of the fit for the data taken during AO2018 expedition. Two example cases are displayed: for a depth of 40 cm at λ = 480 nm and for a 120 cm at λ = 540 nm.

Appendix B

The phase function $p_M(\theta)$ [sr^{-1}] is obtained by consideration of brines and air bubbles scatterers (Malinka et al., 2018). The total phase function is calculated from:

$$p_M(\theta) = \frac{b_b}{b} \cdot p_b(\theta) + \frac{b_a}{b} \cdot p_a(\theta) \tag{B1}$$

$$b = b_b + b_a \tag{B2}$$

where b_b [m^{-1}] and $p_b(\theta)$ [sr^{-1}] refer to the brine scattering coefficient and phase function respectively, while b_a [m^{-1}] and $p_a(\theta)$ [sr^{-1}] are the same quantities for the gaseous inclusions. The total scattering coefficient is given by b [m^{-1}]. The brine channels are optically soft inclusions (relative refractive index ~ 1), large compared to the visible wavelength, and irregular in shape. Hence, their phase function can be described according to (Malinka, 2015):

$$p_b(\theta) = \frac{2x^2(1+\mu^2)}{\left(1+2x^2(1-\mu)\right)^2} \tag{B3}$$

where $\mu = \cos\theta$ and x is the optical size parameter which reduced to $x = 1/(n_b - 1)$ with n_b representing the refractive index of the brine relative to the ice. In the development (Malinka et al., 2018), a value of 1.024 was given for n_b at -2°C (spectrally constant) from formula derived Frisvad (2009). For the air bubble inclusions considered spherical, Mie equations are used with the following size distribution fitted from a power law (Light et al., 2003b):

$$N(r_a) \sim r_a^{-1.5} \qquad 4\ \mu\text{m} \leq \boldsymbol{r_a} \leq 70\ \mu\text{m} \tag{B4}$$

where $N(r_a)$ [Inclusion number·mm^{-3}·µm^{-1}] is the number density at each sphere radius r_a [µm]. The effective phase function is calculated by weighting the phase functions $p_a(\theta, r_a)$ [sr^{-1}] (obtained from Mie computations with a relative refractive index, $n_a = 0.763$) with the corresponding scattering cross-section and number density at each bubble radius:

$$p_a(\theta) = \frac{\int_{r_a=4\ \mu\text{m}}^{r_a=70\ \mu\text{m}} p_a(\theta, r_a) \cdot \pi r_a^2 Q_{scat}(r_a) \cdot N(r_a) \cdot dr_a}{\int_{r_a=4\ \mu\text{m}}^{r_a=70\ \mu\text{m}} \pi r_a^2 Q_{scat}(r_a) \cdot N(r_a) \cdot dr_a} \tag{B5}$$

with $Q_{scat}(r_a)$ representing the scattering efficiency (dimensionless), $\pi r_a^2 Q_{scat}(r_a)$ [µm^2] is the scattering cross-section. To reduce the parameterization of Eq. (B1), the fractional contribution on scattering of the air bubbles over the brines is introduced with the relation

$$\frac{b_a}{b_b} = \frac{R_b}{R_a} \cdot \frac{C_a^v}{C_b^v} \tag{B6}$$

where R_b [µm] and R_a [µm] are the effective radius of the brine and air scatterers respectively (Malinka et al., 2018). The parameter C_a^v/C_b^v (no dimension) is the ratio of volume concentration air-to-brine. The effective radius of bubbles size distribution, Eq. (B4), is $R_a = 42.55$ µm. As for the brines, an estimate of $R_b = 100$ µm is derived from the specific cross-section area values given by Light et al. (2004) (Malinka et al., 2018). We can then determine the total phase function using Eq. (B1) and Eq. (B2) by setting the ratio of volume concentration C_a^v/C_b^v (air-to-brine). The effective average cosine of Eq. (B1), g_M, is determined from:

$$g_M = (1 + b_a/b_b)^{-1} g_b + (1 - (1 + b_a/b_b)^{-1}) g_a \tag{B7}$$

with $g_b = 0.998$, and $g_a = 0.86$ representing the asymmetry parameters of the brines and gas inclusions respectively.

Code availability

All the code used in this study is publicly available at: https://github.com/RaphaelLarouche/radiance_camera_insta360. The repository contains all the scripts for fieldwork data processing and the routines to build the figures of this paper. The codes are undergoing continuous development.

Data availability

Data from RAMSES irradiance sensors taken during AO2018 expedition are available at https://www.meereisportal.de/en/ . They can be retrieved at https://data.meereisportal.de/gallery/index_new.php?lang=en_US&active-tab1=method&active-tab2=buoy&region=all&buoystate=all&buoytype=RB&expedition=Oden_AO18&buoynode=all&submit3=Anzeigen under buoy name 2018R4 (Grosfeld et al., 2016).

Executable research compendium (ERC)

Author contribution

C.K and B.R did the fieldworks and acquired the in-ice measurements presented in this study. S.L.G, C.K and R.L designed the camera calibration and characterization methodologies, while R.L carried them out. B.R, C.K, S.L.G and R.L designed and performed the radiative transfer simulations. R.L and B.R prepared – with equal contribution – the first draft of this manuscript, with inputs from all the authors. S.L.G had the idea to use 360-degree camera inside sea ice and provide help and guidance throughout the project. S.T and M.B supervised the project and provided guidance.

Competing interests

The authors declare that they have no conflict of interest.

Acknowledgements

Raphaël Larouche was supported by the SMAART program through the Collaborative Research and Training Experience program (CREATE) of the Natural Sciences and Engineering Council of Canada (NSERC). This research was supported by the Sentinel North program of Université Laval, made possible, in part, thanks to the funding from the Canada First Research Excellence Fund, the Canadian Excellence Research Chair on Remote sensing of Canada's new Arctic frontier, and Marcel Babin discovery grant #RGPIN-2020-06384. We also gratefully acknowledge the scientific and financial support of Québec-Océan. Field measurements during the AO18 expedition onboard icebreaker Oden were funded by the Helmholtz infrastructure

initiative “FRAM” (Frontiers in Arctic marine Monitoring) and supported by the Swedish Polar Research Secretariat (SPRS). We thank Philipp Anhaus and Mario Hoppmann for assistance in the field. CK was supported by a postdoctoral fellowship from Sentinel North. We would like to thank Anne-Sophie Poulin-Girard for useful inputs regarding calibration methodologies, Marie-Hélène Forget for coordination, Numerical Optics CEO Dr. John Hedley for his generous answers to our countless questions about HydroLight, and Mischa Lavoie for the help during the Chaleur Bay field. Also, we would like to thank Prof. Daniel C. Côté, Yasmine Alikacem, and Christophe Perron for fruitful discussions.

References

Antoine, D., Morel, A., Leymarie, E., Houyou, A., Gentili, B., Victori, S., Buis, J.-P., Buis, N., Meunier, S., Canini, M., and others: Underwater radiance distributions measured with miniaturized multispectral radiance cameras, J Atmos Ocean Technol, 30, 74–95, 2013.

Arrigo, K. R., Sullivan, C. W., and Kremer, J. N.: A bio-optical model of Antarctic sea ice, J Geophys Res Oceans, 96, 10581–10592, 1991.

Arrigo, K. R., Perovich, D. K., Pickart, R. S., Brown, Z. W., van Dijken, G. L., Lowry, K. E., Mills, M. M., Palmer, M. A., Balch, W. M., Bahr, F., and others: Massive phytoplankton blooms under Arctic sea ice, Science (1979), 336, 1408, 2012.

Arrigo, K. R., Perovich, D. K., Pickart, R. S., Brown, Z. W., van Dijken, G. L., Lowry, K. E., Mills, M. M., Palmer, M. A., Balch, W. M., Bates, N. R., and others: Phytoplankton blooms beneath the sea ice in the Chukchi Sea, Deep Sea Research Part II: Topical Studies in Oceanography, 105, 1–16, 2014.

Comiso, J. C.: A rapidly declining perennial sea ice cover in the Arctic, Geophys Res Lett, 29, 11–17, 2002.

Comiso, J. C., Parkinson, C. L., Gersten, R., and Stock, L.: Accelerated decline in the Arctic sea ice cover, Geophys Res Lett, 35, 2008.

Curry, J. A., Schramm, J. L., and Ebert, E. E.: Sea ice-albedo climate feedback mechanism, J Clim, 8, 240–247, 1995.

Ebert, E. E., Schramm, J. L., and Curry, J. A.: Disposition of solar radiation in sea ice and the upper ocean, J Geophys Res Oceans, 100, 15965–15975, 1995.

Edström, P.: A Fast and Stable Solution Method for the Radiative Transfer Problem, SIAM Review, 47, 447–468, https://doi.org/10.1137/S0036144503438718, 2005.

Ehn, J. K. and Mundy, C. J.: Assessment of light absorption within highly scattering bottom sea ice from under-ice light measurements: Implications for Arctic ice algae primary production, Limnol Oceanogr, 58, 893–902, 2013.

Ehn, J. K., Granskog, M. A., Papakyriakou, T., Galley, R., and Barber, D. G.: Surface albedo observations of Hudson Bay (Canada) landfast sea ice during the spring melt, Ann Glaciol, 44, 23–29, 2006.

Ehn, J. K., Mundy, C. J., and Barber, D. G.: Bio-optical and structural properties inferred from irradiance measurements within the bottommost layers in an Arctic landfast sea ice cover, J Geophys Res Oceans, 113, 2008a.

Ehn, J. K., Papakyriakou, T. N., and Barber, D. G.: Inference of optical properties from radiation profiles within melting landfast sea ice, J Geophys Res, 113, C09024, https://doi.org/10.1029/2007JC004656, 2008b.

Ehn, J. K., Mundy, C. J., Barber, D. G., Hop, H., Rossnagel, A., and Stewart, J.: Impact of horizontal spreading on light propagation in melt pond covered seasonal sea ice in the Canadian Arctic, J Geophys Res Oceans, 116, 2011.

Eicken, H., Grenfell, T. C., Perovich, D. K., Richter-Menge, J. A., and Frey, K.: Hydraulic controls of summer Arctic pack ice albedo, J Geophys Res Oceans, 109, 2004.

Frey, K. E., Perovich, D. K., and Light, B.: The spatial distribution of solar radiation under a melting Arctic sea ice cover, Geophys Res Lett, 38, 2011.

Grenfell, T. C.: A theoretical model of the optical properties of sea ice in the visible and near infrared, J Geophys Res Oceans, 88, 9723–9735, 1983.

Grenfell, T. C. and Perovich, D. K.: Radiation absorption coefficients of polycrystalline ice from 400–1400 nm, J Geophys Res Oceans, 86, 7447–7450, 1981.

Grenfell, T. C. and Perovich, D. K.: Seasonal and spatial evolution of albedo in a snow-ice-land-ocean environment, J Geophys Res Oceans, 109, 2004.

Grosfeld, K., Treffeisen, R., Asseng, J., Bartsch, A., Bräuer, B., Fritzsch, B., Gerdes, R., Hendricks, S., Hiller, W., Heygster, G., Krumpen, T., Lemke, P., Melsheimer, C., Nicolaus, M., Ricker, R., and Weigelt, M.: Online sea-ice knowledge and data platform <www.meereisportal.de>, https://doi.org/10.2312/polfor.2016.011, June 2016.

Henyey, L. G. and Greenstein, J. L.: Diffuse radiation in the galaxy, Astrophys J, 93, 70–83, 1941.

Horvat, C., Flocco, D., Rees Jones, D. W., Roach, L., and Golden, K. M.: The Effect of Melt Pond Geometry on the Distribution of Solar Energy Under First-Year Sea Ice, Geophys Res Lett, 47, e2019GL085956, 2020.

van de Hulst, H. C.: Multiple light scattering. Tables, formulas and applications, New York: Academic Press, 1980.

Hunke, E. C., Hebert, D. A., and Lecomte, O.: Level-ice melt ponds in the Los Alamos sea ice model, CICE, Ocean Model (Oxf), 71, 26–42, 2013.

Jacques, S. L.: Optical properties of biological tissues: a review, Phys Med Biol, 58, R37–R61, https://doi.org/10.1088/0031-9155/58/11/r37, 2013.

Jacques, S. L. and Pogue, B. W.: Tutorial on diffuse light transport, J Biomed Opt, 13, 41302, 2008.

Jin, Z., Stamnes, K., Weeks, W. F., and Tsay, S.-C.: The effect of sea ice on the solar energy budget in the atmosphere-sea ice-ocean system: A model study, J Geophys Res Oceans, 99, 25281–25294, 1994.

Katlein, C., Nicolaus, M., and Petrich, C.: The anisotropic scattering coefficient of sea ice, J Geophys Res Oceans, 119, 842–855, 2014.

Katlein, C., Arndt, S., Nicolaus, M., Perovich, D. K., Jakuba, M. v, Suman, S., Elliott, S., Whitcomb, L. L., McFarland, C. J., Gerdes, R., and others: Influence of ice thickness and surface properties on light transmission through Arctic sea ice, J Geophys Res Oceans, 120, 5932–5944, 2015.

Katlein, C., Perovich, D. K., and Nicolaus, M.: Geometric effects of an inhomogeneous sea ice cover on the under ice light field, Front Earth Sci (Lausanne), 4, 6, 2016.

Katlein, C., Arndt, S., Belter, H. J., Castellani, G., and Nicolaus, M.: Seasonal evolution of light transmission distributions through Arctic sea ice, J Geophys Res Oceans, 124, 5418–5435, 2019.

Katlein, C., Valcic, L., Lambert-Girard, S., and Hoppmann, M.: New insights into radiative transfer within sea ice derived from autonomous optical propagation measurements, Cryosphere, 15, 183–198, 2021.

Kattawar, G. W.: A three-parameter analytic phase function for multiple scattering calculations, J Quant Spectrosc Radiat Transf, 15, 839–849, 1975.

Larouche, R., Lambert-Girard, S., Katlein, C., Marty, S., Leymarie, E., Thibault, S., and Babin, M.: On the use of a consumer-grade 360-degree camera as a scientific radiometer, n.d.

Li, Q., Zhou, C., Zheng, L., Liu, T., and Yang, X.: Monitoring evolution of melt ponds on first-year and multiyear sea ice in the Canadian Arctic Archipelago with optical satellite data, Ann Glaciol, 61, 154–163, 2020.

Light, B., Maykut, G. A., and Grenfell, T. C.: A two-dimensional Monte Carlo model of radiative transfer in sea ice, J Geophys Res Oceans, 108, 2003a.

Light, B., Maykut, G. A., and Grenfell, T. C.: Effects of temperature on the microstructure of first-year Arctic sea ice, J Geophys Res Oceans, 108, 2003b.

Light, B., Maykut, G. A., and Grenfell, T. C.: A temperature-dependent, structural-optical model of first-year sea ice, J Geophys Res Oceans, 109, 2004.

Light, B., Grenfell, T. C., and Perovich, D. K.: Transmission and absorption of solar radiation by Arctic sea ice during the melt season, J Geophys Res, 113, C03023, https://doi.org/10.1029/2006JC003977, 2008.

Light, B., Perovich, D. K., Webster, M. A., Polashenski, C., and Dadic, R.: Optical properties of melting first-year Arctic sea ice, J Geophys Res Oceans, 120, 7657–7675, https://doi.org/10.1002/2015JC011163, 2015.

Maffione, R. A., Voss, J. M., and Mobley, C. D.: Theory and measurements of the complete beam spread function of sea ice, Limnol Oceanogr, 43, 34–43, 1998.

Malinka, A., Zege, E., Istomina, L., Heygster, G., Spreen, G., Perovich, D., and Polashenski, C.: Reflective properties of melt ponds on sea ice, Cryosphere, 12, 1921–1937, 2018.

Malinka, A. v: Analytical expressions for characteristics of light scattering by arbitrarily shaped particles in the WKB approximation, JOSA A, 32, 1344–1351, 2015.

Maslanik, J., Stroeve, J., Fowler, C., and Emery, W.: Distribution and trends in Arctic sea ice age through spring 2011, Geophys Res Lett, 38, 2011.

Massicotte, P., Bécu, G., Lambert-Girard, S., Leymarie, E., and Babin, M.: Estimating underwater light regime under spatially heterogeneous sea ice in the Arctic, Applied Sciences, 8, 2693, 2018.

Matthes, L. C., Ehn, J. K., L-Girard, S., Pogorzelec, N. M., Babin, M., and Mundy, C. J.: Average cosine coefficient and spectral distribution of the light field under sea ice: Implications for primary production, Elementa: Science of the Anthropocene, 7, 2019.

Matthes, L. C., Mundy, C. J., L-Girard, S., Babin, M., Verin, G., and Ehn, J. K.: Spatial heterogeneity as a key variable influencing spring-summer progression in UVR and PAR transmission through Arctic sea ice, Front Mar Sci, 7, 183, 2020.

Mobley, C. D.: Light and water: radiative transfer in natural waters, Academic press, 1994.

Mobley, C. D., Cota, G. F., Grenfell, T. C., Maffione, R. A., Pegau, W. S., and Perovich, D. K.: Modeling light propagation in sea ice, IEEE Transactions on Geoscience and Remote Sensing, 36, 1743–1749, 1998.

Morrow, J., Booth, C., Lind, R. N., and Hooker, S. B.: The Compact-Optical Profiling System (C-OPS), NASA Tech. Memo., 42–50, 2010.

Mundy, C. J., Gosselin, M., Ehn, J., Gratton, Y., Rossnagel, A., Barber, D. G., Martin, J., Tremblay, J.-É., Palmer, M., Arrigo, K. R., and others: Contribution of under-ice primary production to an ice-edge upwelling phytoplankton bloom in the Canadian Beaufort Sea, Geophys Res Lett, 36, 2009.

Nicolaus, M. and Katlein, C.: Mapping radiation transfer through sea ice using a remotely operated vehicle (ROV), Cryosphere, 7, 763–777, 2013.

Nicolaus, M., Hudson, S. R., Gerland, S., and Munderloh, K.: A modern concept for autonomous and continuous measurements of spectral albedo and transmittance of sea ice, Cold Reg Sci Technol, 62, 14–28, 2010.

Nicolaus, M., Katlein, C., Maslanik, J., and Hendricks, S.: Changes in Arctic sea ice result in increasing light transmittance and absorption, Geophys Res Lett, 39, 2012.

Pegau, W. S. and Zaneveld, J. R. v: Field measurements of in-ice radiance, Cold Reg Sci Technol, 31, 33–46, https://doi.org/10.1016/S0165-232X(00)00004-5, 2000.

Perovich, D. K. and Gow, A. J.: A quantitative description of sea ice inclusions, J Geophys Res Oceans, 101, 18327–18343, 1996.

Perovich, D. K., Cota, G. F., Maykut, G. A., and Grenfell, T. C.: Bio-optical observations of first-year Arctic sea ice, Geophys Res Lett, 20, 1059–1062, 1993.

Perovich, D. K., Roesler, C. S., and Pegau, W. S.: Variability in Arctic sea ice optical properties, J Geophys Res Oceans, 103, 1193–1208, 1998.

Perovich, D. K., Grenfell, T. C., Light, B., and Hobbs, P. v: Seasonal evolution of the albedo of multiyear Arctic sea ice, J Geophys Res Oceans, 107, SHE–20, 2002.

Perovich, D. K., Richter-Menge, J. A., Jones, K. F., and Light, B.: Sunlight, water, and ice: Extreme Arctic sea ice melt during the summer of 2007, Geophys Res Lett, 35, 2008.

Perron, C., Katlein, C., Lambert-Girard, S., Leymarie, E., Guinard, L.-P., Marquet, P., and Babin, M.: Development of a diffuse reflectance probe for in situ measurement of inherent optical properties in sea ice, Cryosphere, 15, 4483–4500, 2021.

Petrich, C., Nicolaus, M., and Gradinger, R.: Sensitivity of the light field under sea ice to spatially inhomogeneous optical properties and incident light assessed with three-dimensional Monte Carlo radiative transfer simulations, Cold Reg Sci Technol, 73, 1–11, 2012.

Preisendorfer, R. W.: On the existence of characteristic diffuse light in natural waters, 1958.

Preisendorfer, R. W.: Radiative Transfer on Discrete Spaces, Pergamon, v–vi pp., https://doi.org/https://doi.org/10.1016/B978-0-08-010592-5.50003-9, 1965.

Quan, X. and Fry, E. S.: Empirical equation for the index of refraction of seawater, Appl Opt, 34, 3477, https://doi.org/10.1364/AO.34.003477, 1995.

Serreze, M. C., Holland, M. M., and Stroeve, J.: Perspectives on the Arctic's shrinking sea-ice cover, Science (1979), 315, 1533–1536, 2007.

Smith, R. C., Austin, R. W., and Tyler, J. E.: An Oceanographic Radiance Distribution Camera System, Appl Opt, 9, 2015, https://doi.org/10.1364/AO.9.002015, 1970.

Stamnes, K., Tsay, S.-C., Wiscombe, W., and Jayaweera, K.: Numerically stable algorithm for discrete-ordinate-method radiative transfer in multiple scattering and emitting layered media, Appl Opt, 27, 2502–2509, 1988.

Voss, K. J.: Use of the radiance distribution to measure the optical absorption coefficient in the ocean, Limnol Oceanogr, 34, 1614–1622, https://doi.org/10.4319/lo.1989.34.8.1614, 1989.

Voss, K. J. and Chapin, A. L.: Next-generation in-water radiance distribution camera system, in: Ocean Optics XI, 384–387, https://doi.org/10.1117/12.140665, 1992.

Voss, K. J. and Chapin, A. L.: Upwelling radiance distribution camera system, NURADS, Opt Express, 13, 4250, https://doi.org/10.1364/OPEX.13.004250, 2005.

Voss, K. J. and Zibordi, G.: Radiometric and Geometric Calibration of a Visible Spectral Electro-Optic "Fisheye" Camera Radiance Distribution System, J Atmos Ocean Technol, 6, 652–662, https://doi.org/10.1175/1520-0426(1989)006<0652:RAGCOA>2.0.CO;2, 1989.

Wang, H., Chen, Y., Song, H., and Laney, S. R.: A fiber optic spectrometry system for measuring irradiance distributions in sea ice environments, J Atmos Ocean Technol, 31, 2844–2857, 2014.

Warren, S. G., Roesler, C. S., Brandt, R. E., and Curran, M.: Green Icebergs Revisited, J Geophys Res Oceans, 124, 925–938, https://doi.org/10.1029/2018JC014479, 2019.

Wei, J., van Dommelen, R., Lewis, M. R., McLean, S., and Voss, K. J.: A new instrument for measuring the high dynamic range radiance distribution in near-surface sea water, Opt Express, 20, 27024–27038, 2012.

Xu, Z., Yang, Y., Sun, Z., Li, Z., Cao, W., and Ye, H.: In situ measurement of the solar radiance distribution within sea ice in Liaodong Bay, China, Cold Reg Sci Technol, 71, 23–33, https://doi.org/10.1016/j.coldregions.2011.10.005, 2012a.

Xu, Z., Yang, Y., Wang, G., Cao, W., Li, Z., and Sun, Z.: Optical properties of sea ice in Liaodong Bay, China, J Geophys Res Oceans, 117, 2012b.

Supplemental document: In-ice measurements of full spectral angular radiance distributions using a 360-degree camera

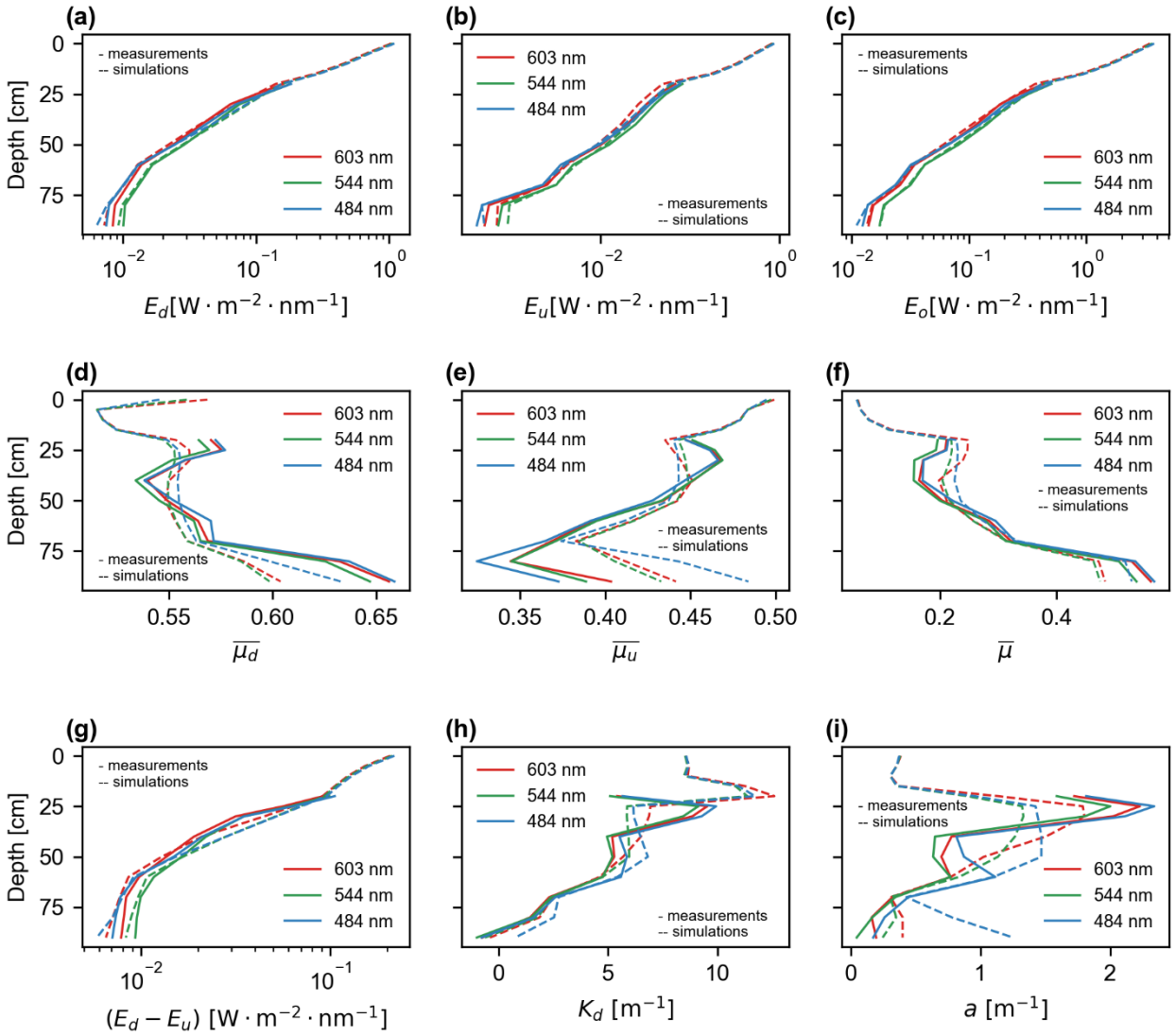

Figure S1: Vertical profiles of planar downward irradiance (a), upward planar irradiance (b), and scalar irradiance for the complete light field angular distribution (c) in Chaleur Bay. The second row shows the average cosines apparent optical properties (AOPs) for respectively (from left to right) the downward, the upward, and the complete radiance values angularly defined. In the last row, we see the net irradiance as a function of the depth in sea ice (g), the diffuse attenuation coefficient for the downwelling irradiance, $\boldsymbol{K_d}$ (in $\mathrm{m^{-1}}$), (h), and the Gershun's Law derived absorption coefficient (i). For each subfigure, the three spectral band curves are displayed according to their colour. The solid lines are the measurement results, while the broken ones are the radiative transfer simulation outputs. Only the field data below the 18 cm freeboard are displayed to allow proper visualization.

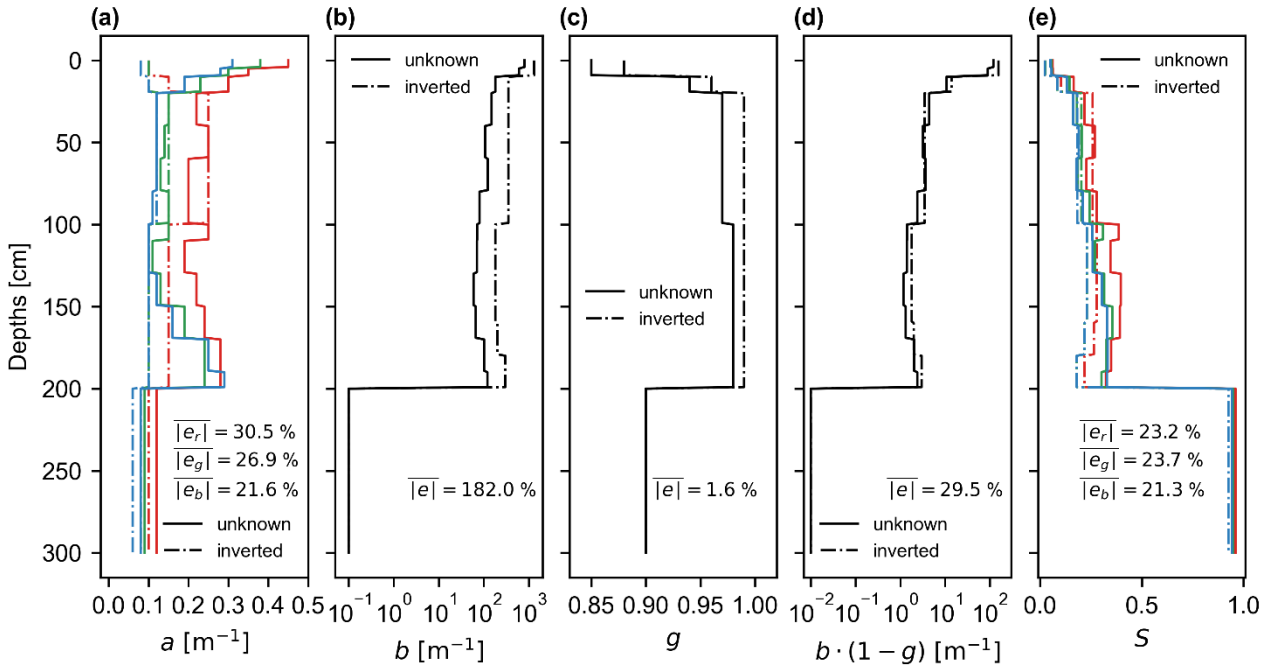

Figure S2: Inherent optical properties inversion errors for multiple layers (13 in total) inside a 200 cm thick sea ice. In order from left to right, the absorption coefficients (a), the scattering coefficients (b), the asymmetry parameter of the Henyey-Greenstein phase function (c), the reduced scattering coefficient (d), and the similarity parameter (e) are presented. The full line corresponds to the IOPs unknown to the expert, while the broken curves are the fitted ones.

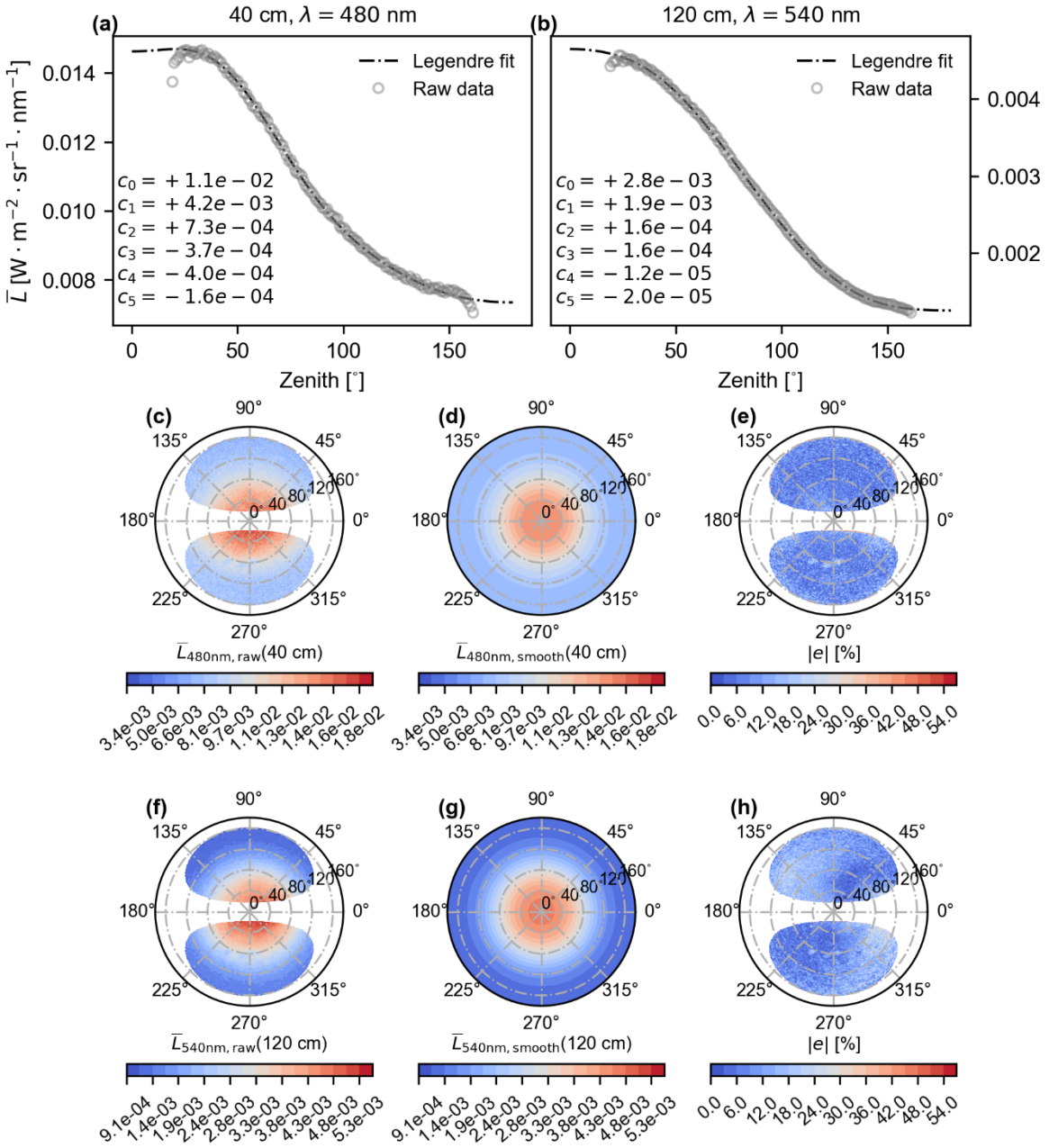

860 **Figure S3:** Legendre polynomials fit results on the azimuthally averaged angular radiance distributions measured in High Arctic. Two radiance distributions example are shown: at a depth of 40 cm and at $\boldsymbol{\lambda}$ = 480 nm, and at 120 cm for the band centered on 540 nm. The first row displays the Legendre polynomials curves fitted over the zenithal radiance (with the Legendre coefficients $\boldsymbol{c_1, c_2, \ldots, c_5}$) for (a) the first and (b) the second case. The second and third rows display (in order of case) the raw angular distributions for all the zenithal and azimuthal

directions (c)-(f), the Legendre polynomials curves re-projected over all the azimuth 360° (d)-(g), and the relative errors between the latter (e)-(h). The average and standard deviation of the relative errors $|\boldsymbol{e}|$ are respectively 6.2 % and 5.4 % for figure (e) and 8.6 % and 6.0 % for figure (h).

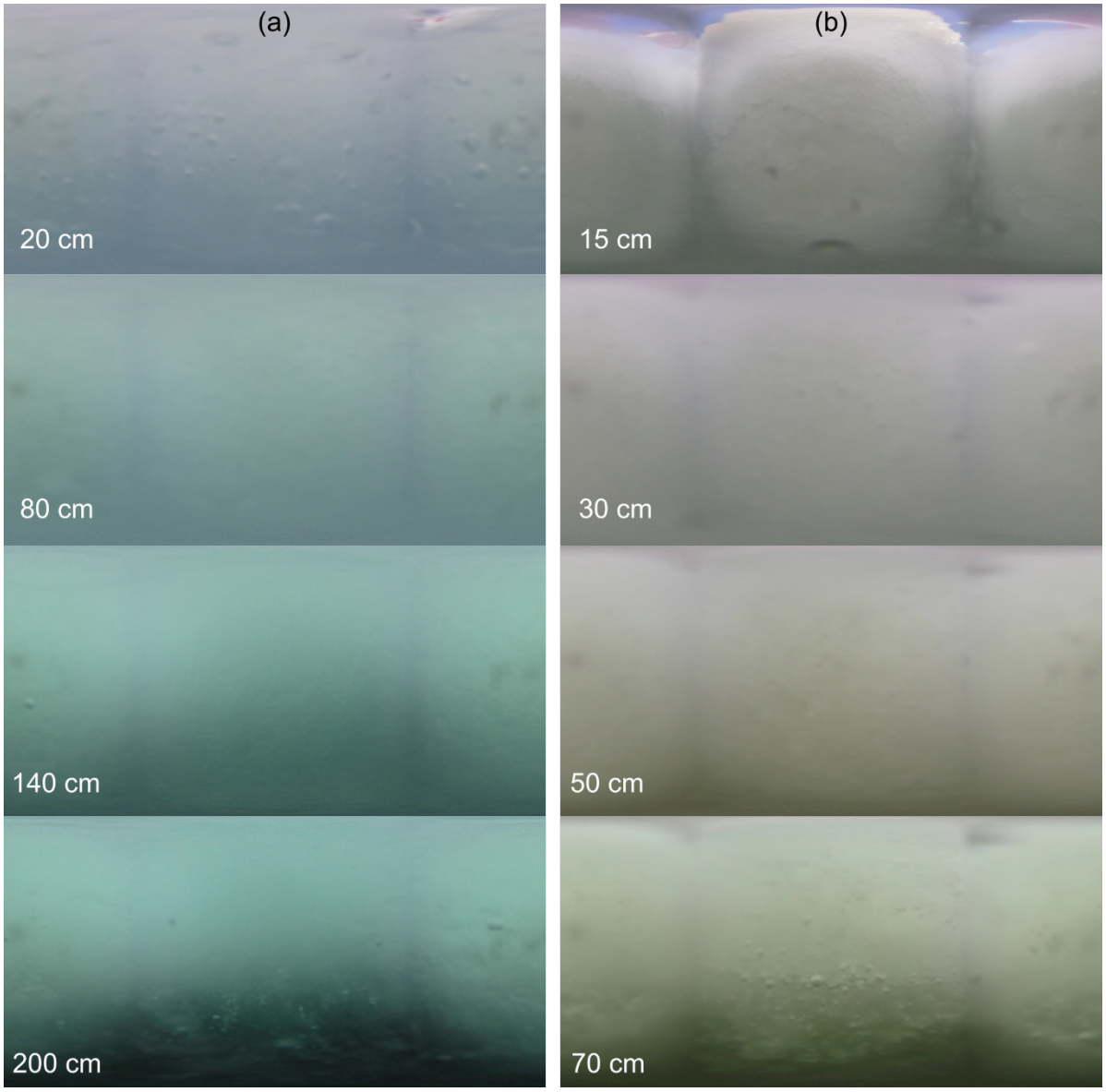

Figure S4: Fisheyes jpeg circular images (saved along DNG raw files) transposed into equirectangular grids. The images are shown column-wise for multiple depths within sea ice at (a) High Arctic (200 cm thick ice) and (b) Chaleur Bay sites (80 cm thick ice). These equirectangular grids have longitudes (FOV in x) x latitudes (FOV in y) less than 360˚ x 180˚ as acquired below the waterlines. We can interestingly observe greener colours in the Chaleur Bay ice (b) compared to bluer ones in Arctic sea ice (a).